# Influence of in situ ceramic reinforcement towards tailoring titanium matrix composites using laser-based additive manufacturing

Kellen D. Traxel and Amit Bandyopadhyay\*
W. M. Keck Biomedical Materials Research Laboratory
School of Mechanical and Materials Engineering
Washington State University, Pullman, WA 99164, USA
E-mail: amitband@wsu.edu

#### **Abstract**

Increasing performance requirements of advanced components demands versatile fabrication techniques to meet application-specific needs. Composite material processing via laser-based additive manufacturing offers high processing-flexibility and limited tooling requirements to meet this need, but limited information exists on the processing-property relationships for these materials as well as how to exploit it for application-specific needs. In this study, Ti/B<sub>4</sub>C+BN composites are developed for high-temperature applications by designedincorporation of ceramic reinforcement (5 wt% total) into commercially-pure titanium to form combined particle and in situ reinforcing phases. We combine both B<sub>4</sub>C (limited reactivity with matrix) and BN (high reactivity with matrix) reinforcements to understand the processing characteristics, in situ phase formations, and combinatorial effect of the multiphase microstructures on thermomechanical properties and high-temperature oxidation resistance. Combined reinforcement in this new composite material leads to superior yield strength and wear resistance in comparison to the other compositions and matrix, as well as comparable oxidation characteristics to commercially-developed high temperature titanium alloys, alleviating the need for multiple rare-earth alloying elements that significantly raises costs for manufacturers. Tubular structures are fabricated to demonstrate the ease of site-specific composition and dimensional tolerancing using this method. Our results indicate that tailored ceramic reinforcement in titanium via laser-based AM could lead to significantly enhanced engineering structures, particularly for developing higher temperature titanium-based materials.

**Keywords:** Directed energy deposition, titanium, boron nitride, boron carbide, oxidation resistance.

### 1. Introduction

Next-generation manufacturing strategies will incite engineers to design components with application-specific material properties, geometry, and functionality—all within a single part. Until now, traditional processing of metallic-based materials has called for machining from large stock pieces, casting for parts with complex features, and/or requiring multi-step techniques for advanced coatings or to achieve other surface functionality. Laser-based additive manufacturing

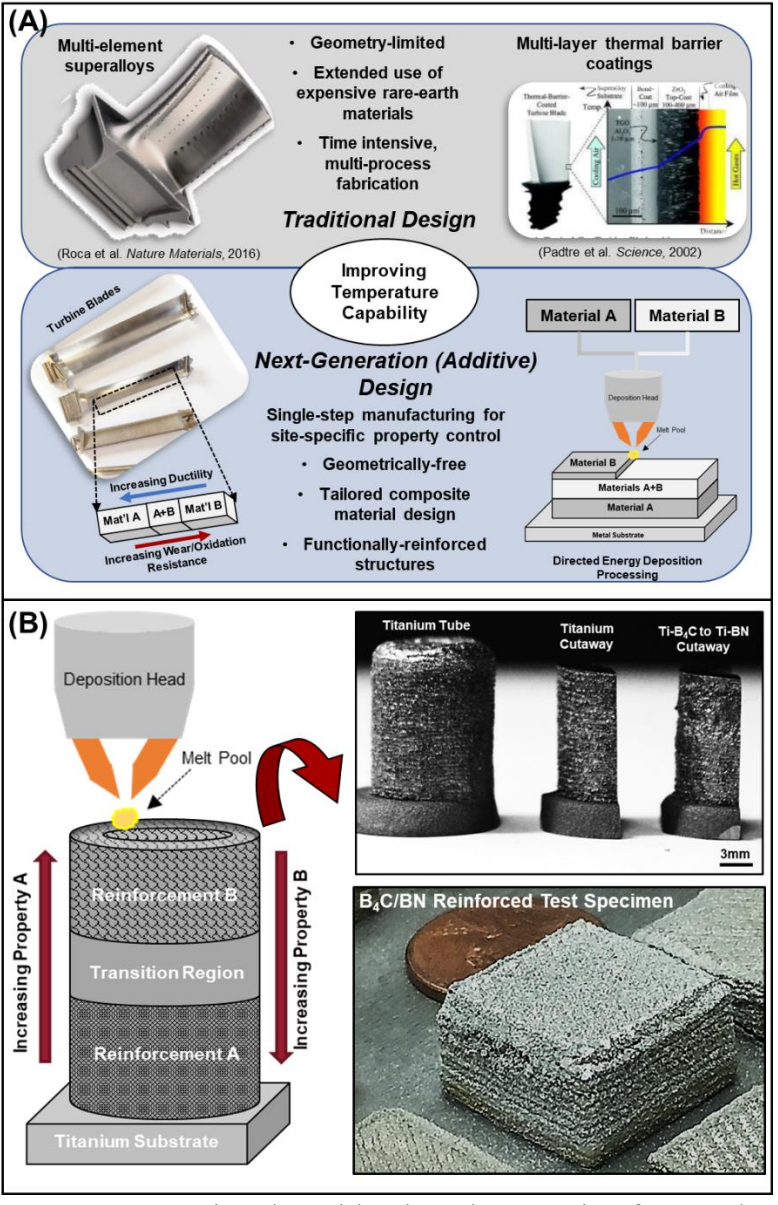


**Figure 1:** Reactive-deposition based processing for metalceramic composites. Reinforcement material and location can be specified and printed by changing the feedstock composition, all with a commercial laser-based AM system.

(AM), or 3D-Printing, has transformed these methodologies by enabling manufacturers to design components in a layer-bylayer fashion, i.e. create from the ground-up, reducing waste material and, in some cases, the need for secondary procedures or post-processing [1–5]. From these efforts, improved engineering alloys have emerged [1–4], as well as multi-material and functionally-graded structures [5– 7], lattice and topology-optimized structures [8,9], and metal-matrix composites and coatings [10–12]. Despite these advances, complex designs still lead engineers to make trade-offs on material and/or geometric features in order to meet specific design criterion. This motivates the expansion of current additive and advanced manufacturing techniques and investigation of novel methods,

particularly in situations where metals that are otherwise unable to perform are desired for use. These situations are commonly found in elevated temperature environments where expensive secondary coatings and/or superalloy materials are used, which significantly increases costs for manufacturers (see Figure 1A). To this end, we demonstrate functional reinforcement manufacturing using directed-energy-deposition (DED), a powder-flow type of metal-AM, to tune the properties of titanium-based metallic materials for use in high-temperature oxidative environments (see Figure 1). DED is a method that is ideal for fabricating multi-material composites by easily changing the printed feedstock material and/or processing parameters, resulting in composites with site-specific composition and performance [1,5]. This aspect opens new design possibilities as metallic or ceramic powders can be strategically printed to form in situ phases and from high-temperature reactions during printing, i.e., reactive-deposition [10,13– 16]. Heat accumulation during processing pushes reactions forward to form refractory phases in situ and provide high-temperature capability to inadequate metals [11,17–19]. Examples of these phases include metal borides and carbides/nitrides which form in situ from metal and ceramic powders, or act as particle reinforcement within the metallic matrix. This reinforcement technique is more direct in comparison to traditionally-produced multi-element superalloys, or components with multi-step coatings and composites that require complex processing equipment and too complex of geometry (Fig. 1A). It is envisioned that reactive-deposition can be implemented as a single step manufacturing process for high-temperature applications such as location-specific coatings and/or bulk structures in high temperature/wearing regions.

Titanium-based components, in particular, maintain relatively low operating temperature (400°C-500°C) and wear resistance despite having desirable strength/weight ratio and corrosion resistance for many applications in aerospace, nuclear, marine, and biomedical industries [20]. Among many others, alternative materials such as titanium aluminides have historically been investigated for replacing nickel-based or other high-temperature superalloys in areas where the operating temperature is too high for titanium, but ductility plays a role in fabricability challenges that typically include complex heat treatment steps [21,22]. In addition, methods such as powder metallurgy [23,24], spark plasma sintering [25], deposition-based coatings [26], and tape-based or other casting methods [27,28], among others, have been investigated to reinforce titanium but suffer from low geometric freedom, flexibility of reinforcing strategies, and are limited to single material or composition. From this, it is envisioned herein that improvements in

properties could be made by small (<5wt%) functional reinforcement of ceramic (and subsequent in situ phases) for site-specific composite properties, and printed with the reactivity of feedstocks in mind for tailoring the resulting microstructure and properties. To this end, titanium composites with B<sub>4</sub>C/BN ceramic reinforcement were manufactured using DED-based processing to understand the effect of ceramic on properties as well as reinforcement strategy. Boron nitride (BN) was chosen for its previous ability to increase the wear resistance and hardness of the titanium matrix through its reactivity and propensity to form TiN and TiB [16,29], and boron carbide (B<sub>4</sub>C) was chosen for its ability to significantly improve the strength of the titanium matrix through particle reinforcement. Because of the limited information on high-temperature oxidation performance of these composite materials through laser-based processing, isothermal oxidation testing was performed to understand the scale formation and effect on weight change in an elevated temperature environment. To the best of our knowledge, no work exists on functionally reinforcing titanium composites in a single manufacturing step with multiple reinforcing agents, as well as limited information on the high-temperature oxidation resistance of these class of structures, which differentiates the current work. It was hypothesized that the formation of ceramic phases from combined particle and in situ phase formation would result in a composite with improved resistance to oxidation while maintaining significantly improved properties over the matrix material, titanium. To evaluate this hypothesis, four different compositions (CPTi, CPTi-5wt%B4C, CPTi-5wt%BN, CPTi-2.5wt%B4C-2.5wt%BN) were printed separately, as well as demonstration pieces with multiple transition strategies. The CPTi composition (commercially-pure titanium, also referred to in this work as "Ti") serves a control for studying the base-material (or matrix) performance, whereas the BN and B<sub>4</sub>C reinforced compositions serve to understand the effect of the different reinforcement on microstructure and thermomechanical properties. The final composition (CPTi-B<sub>4</sub>C-BN) was used to evaluate the combined effect of ceramic reinforcements on overall properties while maintaining the same overall reinforcement amount. Isothermal oxidation testing, quasi-static compression, reciprocating wear, and thermal diffusivity testing were used to understand the individual composites' properties in comparison to the titanium matrix. Scanning electron microscopy (SEM), X-ray diffraction (XRD), and Gibbs free energy change analysis were used to understand the phase evolution and microstructural features that occur during processing. Our

work demonstrates the ability to functionally reinforce ineffective materials to achieve application-optimization using a commercially-available additive manufacturing process.

.

## 2. Materials and methods

2.1 Reactive-deposition based processing and dimensional expansion measurements: Our LENS<sup>TM</sup> system (Optomec LENS<sup>TM</sup> 750, Optomec, Albuquerque, NM) operates a continuouswave, Nd:YAG laser (500W) that focuses a beam on top of a substrate that is moved in the x/y directions to outline the CAD cross section while powder is simultaneously fed into the melt pool. The buildplatte is contained in an argon environment ( $O_2$  ppm < 15). The powder composition is carried into the melt pool via an argon stream. Further discussion can be found in references [11,30]. Spherical CPTi powder (Gr.2 Ancor-Ti, Hoganas, Sweden), granular-B<sub>4</sub>C powder (Presi, Switzerland), and hexagonal-BN powder ("PTX60" from Momentive Performance Materials, Waterford, NY) were obtained for printing of the composite structures. Titanium powder was printed within a 45-150µm particle size range, and the ceramic particles ranged from 25-75µm in overall size (after sieving). The premixed composition was milled for 20 minutes, without balls, to ensure compositional homogeneity. Because these powders are of different color (titanium-gray, B<sub>4</sub>C-black, and BN-white), it was clear after 20 minutes of milling the composition was evenly distributed throughout the container as there were no regions of white or black throughout the container. All samples were 3D printed separately as 15mm by 25mm rectangular cross-sectional patterns, onto a 3.4mm thick CPTi substrate, according to the parameters outline in Table 1. Four compositions (CPTi, CPTi-5wt%B4C, CPTi-5wt%BN, CPTi-5wt%B4C-5wt%BN) were 3D printed separately on the same build-plate (Optomec LENS<sup>TM</sup> 750, Optomec, Albuquerque, NM). The first composition (CPTi) serves as the primary control, whereas the second and third compositions (CPTi- CPTi-5wt%B4C & CPTi-5wt%BN, respectively) were chosen to evaluate the effect of B<sub>4</sub>C and BN on the LENS<sup>TM</sup>-processed CPTi system. The final composition (CPTi-5wt%BAC-5wt%BN) was determined by preserving a 5wt% reinforcement to the titanium matrix while combining the two separate reinforcements. Optimized laser-power and scan settings are shown in Table 1. Parameters needed to be adjusted to accommodate the different reinforcements, which affected the layer thicknesses. Our goal was to match the layer thickness as closely as possible to indicate the feasibility of making functional

components out of these compositions. Dimensions of the first set of block samples were measured using digital caliper ( $\pm 0.01$  mm) and compared to CAD design. Percent expansion was calculated as:

% Expansion = 100% 
$$\left[\frac{L_{total} - L_{CAD}}{L_{CAD}}\right]$$
 (1)

Where  $L_{total}$  is the measured specimen length, and  $L_{CAD}$  represents the CAD-based dimension. A precision error of 2.5% was considered when calculating values, due to the tendency of DED-based processes to provide edge-effects that increase the overall final part dimension(s) [16].

2.2 Sample preparation, microstructural characterization, and phase analysis Samples for imaging and analysis (**Figs. 2 & 3**) were sectioned from the as-printed structures via low-speed diamond saw, mounted in phenolic resin, then sequentially wet-ground using 60-2000 grit SiC paper. Polishing was performed using an alumina-DI water suspension on polishing pad from 1μ down to 0.05μ. X-Ray Diffraction (XRD) (X'Pert PRO PANalytical, Almelo, Netherlands, Cu Kα source and a Ni filter) was performed for the as-printed specimens (**Fig. 4**). All intensities were normalized by the largest peak observed. Vickers cross-section hardness indents (Phase II, Upper Saddle River, NJ) were taken in line with ASTM standards for both metals and advanced ceramics on the unetched, ground and polished samples in the as-processed and oxidized conditions [31,32]. High-magnification microstructural imaging, Field-Emission Scanning Electron Microscopy (FESEM, SEM) was utilized on both etched as-printed specimens, as well as unetched compression-tested samples. Submersion etching for 25s was done in Kroll's Solution (92mL DI Water, 6mL HNO<sub>3</sub>, & 2mL HF).

2.3 Isothermal oxidation: Oxidation measurements and analysis were performed to understand the effect of composition on mass gain and kinetics (**Figs. 5-8**). Weight-change measurements for the oxidized samples (all compositions) were performed using a Netsch STA 409-PC Luxx unit (Burlington, MA). A single sample from each composition was loaded in an alumina crucible and contained with a lid with a central hole, and the sample dynamically weighed under air delivery (accuracy of 0.01mg). A heating rate of 20°C/min was used to reach isothermal testing temperature, hold time of 25hrs., and then a 40°C/min decrease back down to room temperature. During measurement, air at 0.5psig and flow rate of 40 mL/min was supplied.

Optical microscopy was used to analyze the surface scale (Fig. 6) and scale thickness (Fig. 8). Arrhenius analysis (Fig. 7) was carried out according to the fundamental mass change relationship:

$$\left(\frac{\Delta W}{A}\right)^n = K_{l,p}t \quad (2)$$

Where  $\Delta W$  represents the mass change, A is the exposed surface area, and  $K_{l,p}$  is the rate constant given in units of (mgcm<sup>-2</sup>s<sup>-1</sup>) for linear kinetics where n=1, and units of (mg<sup>2</sup>cm<sup>-4</sup>s<sup>-1</sup>) for parabolic kinetics where n=2. After identifying the proper  $K_{l,p}$  term based on the kinetic characteristics, the Arrhenius relationship can be used:

$$K_{l,p} = K_0 exp\left(-\frac{Q}{RT}\right) \quad (3)$$

Where  $K_0$  is a constant, Q the activation energy in kJmol<sup>-1</sup>, R the universal gas constant, and T the absolute temperature. This equation can be re-written as such:

$$\log (K_p) = \log (K_0) - \frac{Q}{2.303R} * \left(\frac{1}{T}\right) \quad (4)$$

From which experimentally-determined (**Table 3**) values for  $K_p$  and  $\frac{1}{T}$  can be plotted and Q evaluated by taking the slope of the line and equating it to  $\frac{Q}{2.303R}$ , with the 2.303 factor used for the logarithm change of base.

2.4 Thermomechanical testing: Quasi-static compression testing (Shimadzu, Trapezium X, Kyoto, Japan) was performed at constant displacement rate of 0.15 mm/min (~0.2\*10<sup>-4</sup> s<sup>-1</sup> strain rate in linear region) until plastic deformation was evident from the live displacement vs. force output (**Figs. 10-11**). Two samples per configuration were ground to side-lengths of 5.25±0.05mm and height of 11.5±0.05mm for an average aspect ratio of ~2. Moduli were evaluated via slope of the stress-strain curve, and a standard 0.2% offset method was used to calculate yield strength, per ref. [33]. Damage analysis via SEM was performed on a single ascompressed, unetched sample from each configuration (**Fig. 11**). Thermal diffusivity testing was performed via the flash method from 50°C-300°C (NETZSCH, Germany) on specimens measuring 10.4±0.5mm square and 2.5±0.05mm thickness that were cut from the as-printed structures. Prior to testing, a thin layer of graphite was applied on each side of the testing

specimen to ensure measurement accuracy. Five separate tests were performed at each temperature value. Wear degradation testing (NANOVEA, Irvine, CA) was performed according to ASTM standard on flat sliding wear to determine the coefficient of friction (COF) and compound wear rate (**Fig. 11**) [34]. Testing conditions were a 1000m distance test at a load of 10N, track length of 10mm, 3mm diameter Al<sub>2</sub>O<sub>3</sub> wear-ball, DI water medium at ambient conditions, and test rate of 1Hz (1200 mm/min linear wear speed). COF and wear depth were collected during testing, and three separate tests were performed on each composition at 7N. The COF plots shown are from a single run from each composition, and are representative of each composition's characteristics over the course of the test. Compound wear rate was evaluated using the final wear depth after 1000m, using the equation below from [34]:

Wear Volume = 
$$\left(\frac{\pi h}{6}\right) \left[\frac{3D^2}{4+h^2}\right]$$
 (5)

With:

$$h = R - R \sqrt{R^2 - \frac{D^2}{4}}$$
 (6)

Where *R* is the wear-ball radius, *h* is the scar height, and *D* is the wear track length. Normalized value was obtained by dividing by both the distance and the load.

#### 3. Results

Ti-B<sub>4</sub>C-BN composites were successfully processed using laser-based additive manufacturing, leveraging reactive-deposition to form *in situ* reinforcing phases. Isothermal oxidation, compression, thermal diffusivity, and reciprocating wear testing were used to characterize the performance of these composites.

3.1 Reactive-deposition based processing and dimensional-expansion measurements: All four compositions were printed using similar geometry (16mm x 25mm rectangular), hatching sequence (0°, 120°, 240°, 180°), and spacing between deposits (0.58mm, approx. 40% deposit overlap), but power and scanning speed were tuned to optimize the amount of deposited material per layer and minimize visible defect phenomena such as balling and unwanted porosity, as shown in **Table 1**.

**Table 1:** Processing parameters for LENS<sup>TM</sup> deposited Ti-B<sub>4</sub>C-BN coatings and structures.

Composition	Laser Power (W)	Hatch Scan Speed (mm/s)	Contour Scan Speed (mm/s)	Hatch Spacing (mm)	Layer Thickness (µm)	Hatch Angle Sequence	Relative Density
CPTi	350	6.7	5.0		400	Layer 1:	96.4%±2%
CPTi-5B <sub>4</sub> C	410	6.4	4.5		415	0° Layer 2:	97.4%±2%
CPTi-5BN	450	6.4	4.0	0.58	375	120°	96.1%±2%
CPTi-2.5B <sub>4</sub> C- 2.5BN	450	6.0	4.0	Layer 3: 240° Layer 4: 180°	410	96.3%±1%	

After the first layer was optimized, the scanning speed and power remained constant for all subsequent layers. CPTi was processed at the lowest power of 350W and a scanning speed of 5.0 mm/s and 6.7 mm/s for the contour and hatch, respectively. For the ceramic-containing compositions, limited deposit height was exhibited for 350W, so the energy input was increased by both increases in power (410W-450W) as well as decreased scanning speed (4.0mm/s-6.0mm/s). These processing conditions resulted in layer thickness of ~375-415μm and dimensional expansion of ~15%-17% relative to the X-CAD dimension, and ~17-19% for the Y-CAD dimension (see **Table 2**), indicating that component part height and features are repeatable even with the addition of 5wt% ceramic phase.

**Table 2:** Percent expansion of all compositions from CAD-to-part for the as-built compression samples. Machine "edge" error was considered within the calculations.

Composition	Parameter	X (CAD:16mm)	Y (CAD:25mm)
100% CPTi	Measured Dimension % Expansion	19.3±0.03 18.3%	28.9±0.23 15.3%
CPTi-5B <sub>4</sub> C	Measured Dimension % Expansion	19.4±0.09 18.9%	29.3±0.23 16.7%
CPTi-5BN	Measured Dimension % Expansion	19.4±0.01 18.9%	29.1±0.14 16.0%
CPTi-2.5B <sub>4</sub> C-2.5BN	Measured Dimension	19.3±0.09	29.3±0.13

3.2 Microstructure and phase analysis: All as-printed surfaces were free from cracking and large-scale defects, and the hatching directions can be distinctly visualized from Figs. 2A1-2D1. In addition, the etched microstructures (Figs. 2A2-2D2) were free from large-scale cracking and processing-induced defects, but differed significantly in the phases present.

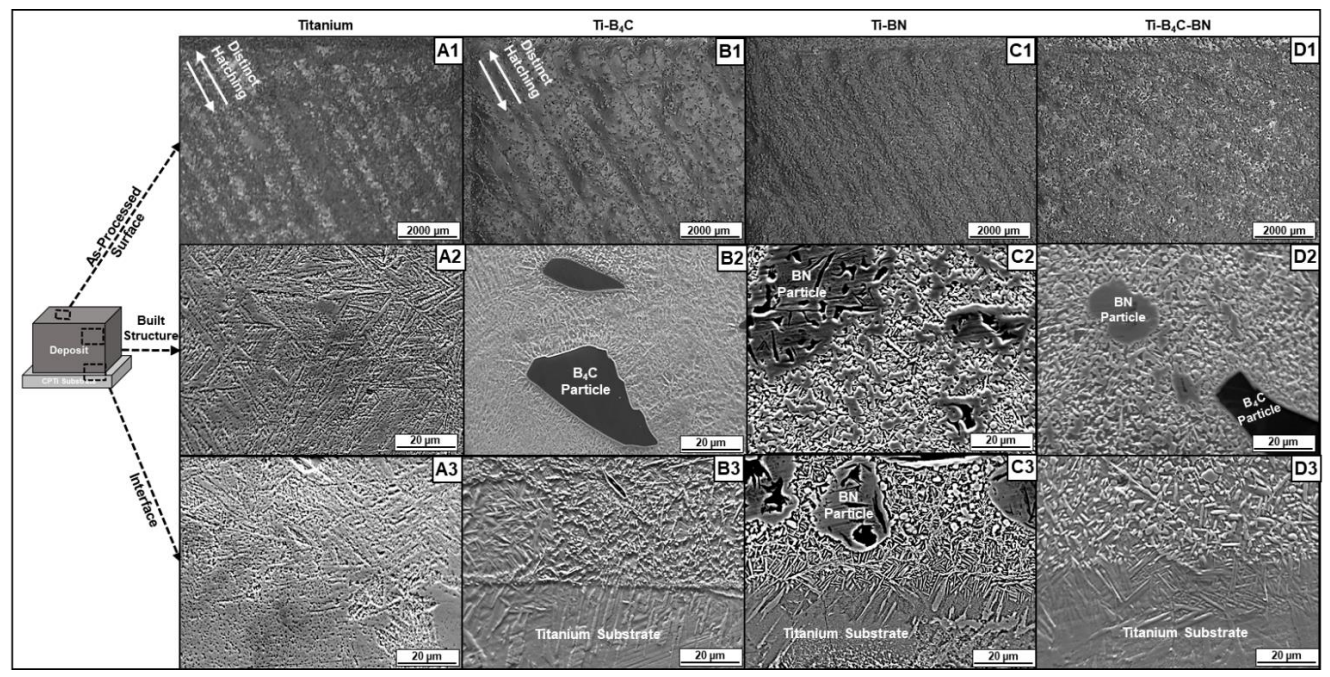


**Figure 2:** As-printed surface morphology and etched-microstructures of each composite within the bulk sample as well as at the interface. **(A)** Titanium **(B)** CPTi-B<sub>4</sub>C **(C)** CPTi-BN **(D)** CPTi-B<sub>4</sub>C-BN.

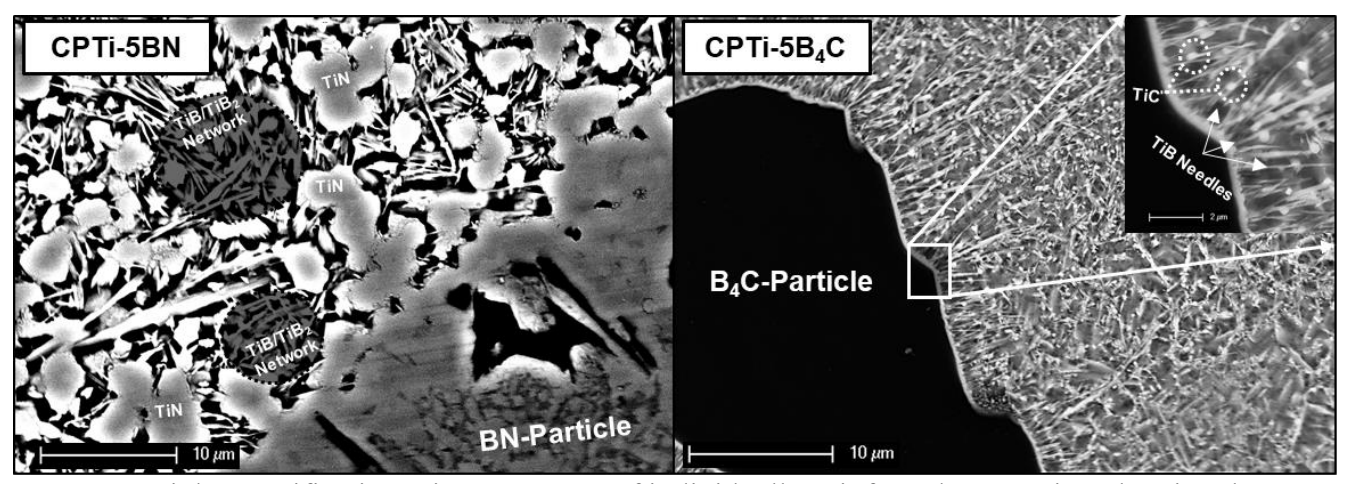


**Figure 3:** High-magnification microstructures of individually-reinforced composites showing the nature of the reaction zones around each of the individual reinforcements.

The CPTi composition mainly consisted of α-phase (HCP) Widmanstatten microstructures typical of AM-produced titanium, with a diffuse transition from the CPTi substrate to the as-printed material (Fig. 2A3). This was consistent with the main  $\alpha$ -phase peaks at  $47^{\circ}$  and  $45^{\circ}$ (ICSD:52522) as shown in the XRD analysis (Fig. 4). These peaks were observed in each of the ceramicreinforced compositions,

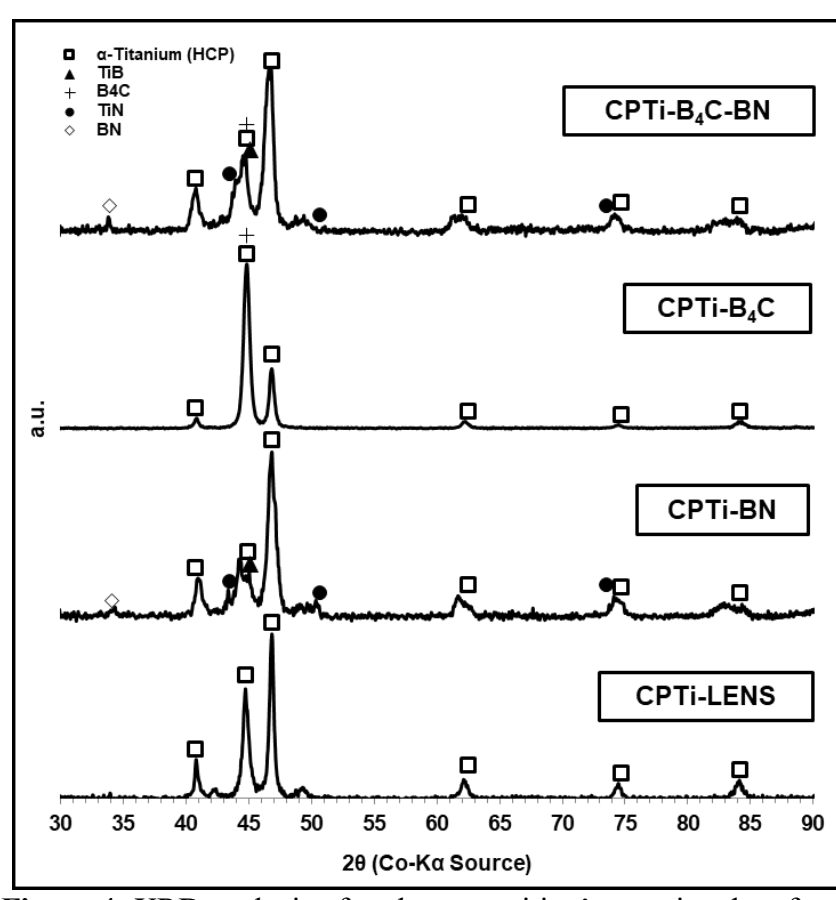
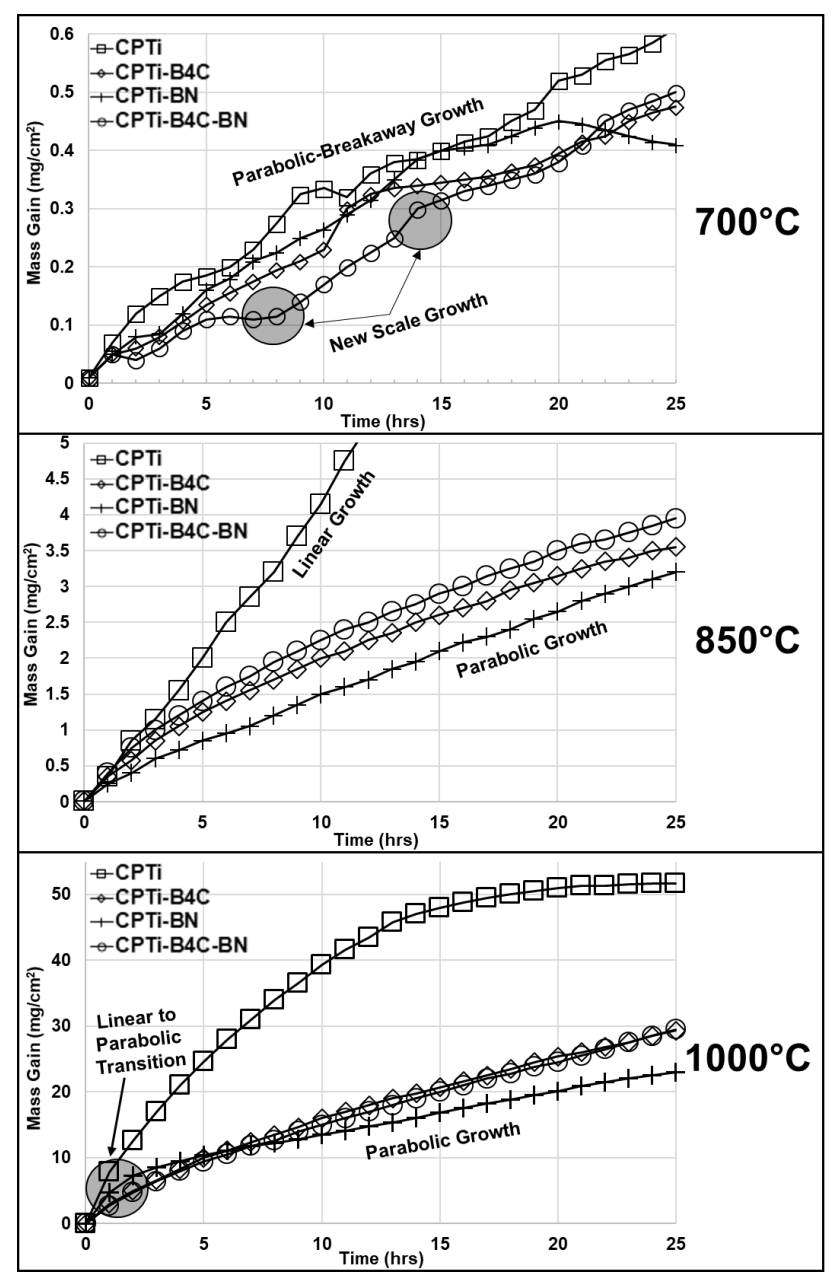


Figure 4: XRD analysis of each composition's as-printed surface.

which all had distinct transitions from the substrate to the as-printed material as indicated in (Figs. 2B3-2D3). The CPTi-5B4C composition (Fig. 2B2) was comprised of a primary α-phase (HCP) titanium matrix with B4C particles dispersed from 20-50μm, which is the only other phase observed in the XRD analysis (ICSD:654971), overlapping with the 45° titanium peak. Higher magnification images reveal the reaction zone comprised of a dual TiC-TiB reinforcement region immediately adjacent to the B4C particles, but mostly titanium in the matrix region, which has been previously reported [35], but was not observed in the XRD analysis. These features indicate that this composition is predominately particle-reinforced as opposed to *in situ* phase reinforced. The CPTi-5BN composition exhibited a microstructure predominantly comprised of TiN dendrites and TiB/TiB<sub>2</sub> networks interspersed between the TiN phase, as has been reported in other works [12,16,29], indicating that this composition is highly *in situ* phase reinforced. Additionally, BN particles that are partially reacted (20-75μm) with the titanium matrix are observed with some internal porosity within the particles. The XRD analysis shows the presence of TiN at 48° (ICSD:183415), TiB at 45° (ICSD:24701), and BN at 34° (ICSD:162875), in

addition to titanium, which corroborates the dominant microstructural features found via SEM imaging. Further, the CPTi-B<sub>4</sub>C-BN composite maintained a microstructure that was a combination of the two individually-reinforced compositions. Partially-reacted BN particles along with B<sub>4</sub>C particles are readily observed within the microstructure, as well as the networks of TiB/TiB<sub>2</sub> and TiN dendrites, indicating that both ceramic feedstocks are reacting with the titanium matrix during deposition. For all compositions, the microstructural features at the interface were similar in nature to the features within the bulk sample, indicating that the heat accumulation effect common to DED-based processing was minimal on the microstructural features of the composites.

3.3 Isothermal oxidation: **Figs. 5-8** display the results of isothermal oxidation testing of the composites from 700°C-1000°C. For all compositions, XRD analysis (**Fig. 7A**) of the 1000°C tested surfaces revealed exclusively TiO<sub>2</sub> in the form of rutile (tetragonal structure),



**Figure 5:** Isothermal-oxidation weight change curves for 700°C, 850°C, and 1000°C across the 25-hr test, with the kinetic characteristics identified.

indicating that the sole oxidation product was TiO<sub>2</sub> (Rutile ICSD: 9161). This is substantiated further by the derivative of the Arrhenius plots (Fig. 7B) which reveled activation energies for oxidation ranging from 127-167 kJmol<sup>-1</sup> for all compositions. These values remained consistent across temperature for each composition, and are very near to the activation energy range previously reported for TiO<sub>2</sub> (88-276 kJmol<sup>-1</sup>) [21,36,37], indicating that the driving factor for mass change in these composites at high temperature is the oxidation of the titanium matrix and diffusion of oxygen through the scale.

Figure 5 displays the weight change curves normalized by surface area for each of the compositions at all

temperatures, and **Table 3** provides fit parameters for either parabolic or linear kinetic regimes. Surface scale micrographs are shown in **Figure 6** with the corresponding scale thickness shown

in Fig. 8A. At 700°C, all compositions exhibited parabolic-breakaway schemes throughout the entirety of testing, whereas, at 850°C the regimes were strictly linear for CPTi and parabolic for all ceramic-reinforced composites. At 700°C, the K<sub>p</sub> values are decreased as much as 31% from  $9.20e^{-2}$  (mg<sup>4</sup>cm<sup>-4</sup>s<sup>-1</sup>) down to  $7.0e^{-2}$  (mg<sup>4</sup>cm<sup>-4</sup>s<sup>-1</sup>) with the addition of B<sub>4</sub>C, and 21% with the addition of BN, which remained the same for the CPTi-B<sub>4</sub>C-BN composition. Further, the scale on the CPTi surface is fully spread and covering most of the original grinding lines, whereas the scales on the ceramic compositions are either still spreading outward (CPTi-B<sub>4</sub>C), or fully spread at significantly lower overall thickness (CPTi-BN and CPTi-B<sub>4</sub>C-BN). Further, the scale thickness was significantly reduced from 2.9±0.4μm to as low as 1.6±0.2μm in the case of CPTi-B<sub>4</sub>C-BN composition (45% decrease), and a 31-38% decrease with the addition of BN and B<sub>4</sub>C alone, respectively. All compositions were free from cracking and large-scale spallation. At 850°C, the kinetic regime shifts from linear to parabolic with the addition of ceramic. K<sub>p</sub> values ranged from 0.27-0.38 (mg<sup>4</sup>cm<sup>-4</sup>s<sup>-1</sup>) for B<sub>4</sub>C and BN reinforcement, with the CPTi-BN composition exhibiting the lowest value. An order of magnitude increase in the K<sub>p</sub> values when comparing from 850°C to 700°C is attributed to the higher temperature and propensity for reaction with the oxidizing environment. From the scale micrographs (Fig. 6), it is seen that during the 25hr period, the CPTi scale not only grew on the surface but also outward from the surface in certain areas. The scale thickness significantly decreased from 123.4±9.3µm to 12.5±2.0µm for CPTi-B<sub>4</sub>C, 19.3±5.3µm for CPTi-BN, and 15.0±1.4µm for CPTi-B<sub>4</sub>C-BN (overall 7X decrease in scale thickness compared to CPTi). The CPTi-B<sub>4</sub>C and CPTi-B<sub>4</sub>C-BN compositions both exhibited smooth even scales, whereas the CPTi-BN composition showed areas of outward growth as well as dispersed throughout the surface. All compositions were free from cracking and large-scale spallation. At 1000°C testing level, there was a transitional kinetic regime from linear to parabolic for all compositions, varying from 1.5hrs-2.5hrs depending on the composition. K<sub>p</sub> values for CPTi were 7.10 (mg<sup>2</sup>cm<sup>-2</sup>s<sup>-1</sup>) for the linear regime (0-1.5hrs) and 9.49 (mg<sup>4</sup>cm<sup>-4</sup>s<sup>-1</sup>) for the parabolic regime. With the addition of B<sub>4</sub>C, these values decreased to 1.26 (mg<sup>2</sup>cm<sup>-2</sup>s<sup>-1</sup>), 2.67 (mg<sup>4</sup>cm<sup>-4</sup>s<sup>-1</sup>) for the linear and parabolic regimes, respectively (4.7X and 2.6X decreases). For the CPTi-BN composition, the values decreased to 4.98 (mg<sup>2</sup>cm<sup>-2</sup>s<sup>-1</sup>), 6.04 (mg<sup>4</sup>cm<sup>-4</sup>s<sup>-1</sup>) for the linear and parabolic regimes, respectively (43% and 57% decreases). For the combined composition (CPTi-B<sub>4</sub>C-BN), values decreased to 2.05 (mg<sup>2</sup>cm<sup>-2</sup>s<sup>-1</sup>), 2.75 (mg<sup>4</sup>cm<sup>-4</sup>s<sup>-1</sup>) for the linear and parabolic regimes, respectively (2.5X decrease for both regimes).

**Table 3:** Isothermal oxidation characteristics of the titanium composites

T(0C)	T(°C) Composition	Oxidation	Fit Parameters			
1(°C)	Composition	Characteristics	*KL, Kp	N	R <sup>2</sup> Value	
	CPTi		9.20e <sup>-2</sup>	1.8	0.98	
<b>7000</b> C	CPTi-B <sub>4</sub> C	Parabolic-	7.00e <sup>-2</sup>	1.8	0.93	
700°C	CPTi-5BN	Breakaway	7.60e <sup>-2</sup>	1.8	0.94	
	CPTi-2.5B <sub>4</sub> C-2.5BN		7.60e <sup>-2</sup>	1.8	0.86	
	CPTi	Linear	0.51	1.0	0.99	
850°C	CPTi-5B4C		0.34	1.4	0.99	
	CPTi-5BN	Parabolic	0.27	1.4	0.99	
	CPTi-2.5B <sub>4</sub> C-2.5BN		0.38	1.4	0.99	
	СРТі	Linear to Parabolic (1.5hr to transition)	7.10, 9.49	1.0, 1.8	0.99, 0.97	
100000	CPTi-5B4C	Linear to Parabolic (2.5hr to transition)	1.26, 2.67	1.0, 1.4	0.99, 0.99	
1000°C	CPTi-5BN	Linear to Parabolic (1.5hr to transition)	4.98, 6.04	1.0, 2.4	0.99, 0.99	
	CPTi-2.5B4C-2.5BN	Linear to Parabolic (2.5hr to transition)	2.05, 2.75	1.0, 1.4	0.99, 0.99	
*for line	ear kinetics fit units of K <sub>p</sub>	(mg*cm <sup>-2</sup> s <sup>-1</sup> ), whereas p	parabolic kinet	ic fit units of K	$(mg^2cm^{-4}s^{-1})$	

Further, the scale for the CPTi sample reached 664.9±15.1µm and was effectively decreased

with the addition of B4C by 1.8X to 240.6±74.1μm, 2.5X to 190.5±10.8μm with the addition of BN, and 1.8X for CPTi-B4C-BN to 237.1±31.7μm. The CPTi scale exhibited significant outward growth from the surface as indicated from **Fig. 6**. The CPTi-BN composition exhibited outward growth in much lower scale than was exhibited by CPTi, and the CPTi-B<sub>4</sub>C and CPTi-B<sub>4</sub>C-BN compositions exhibited scale growth on the surface with minimal visible outward growth. All compositions were free from cracking and large-scale spallation. **Fig. 8B** displays the bulk hardness values for each composition that were tested for 25hrs that were measured 1.5mm (halfway) through the sample cross-section. CPTi demonstrated an as-processed hardness of 274±8HV<sub>0.2/15</sub>, with a decrease to 157±9HV<sub>0.2/15</sub> and 143±6HV<sub>0.2/15</sub> for the 700°C and 850°C

temperatures. The bulk hardness increased to 322±70HV<sub>0.2/15</sub>, however, when tested at 1000°C. The CPTi-B<sub>4</sub>C composition remained relatively stable with slight increases in average hardness from an as-processed condition of  $348\pm31 \text{HV}_{0.2/15}$  to  $377\pm25 \text{HV}_{0.2/15}$ ,  $385\pm17 \text{HV}_{0.2/15}$  and 465±51HV<sub>0.2/15</sub> for 700°C, 850°C, and 1000°C temperatures. There was a much more significant increase in hardness for the CPTi-BN composition from an as-processed condition of  $713\pm85$ HV<sub>0.2/15</sub> to  $774\pm116$ HV<sub>0.2/15</sub>,  $981\pm102$ HV<sub>0.2/15</sub> and  $920\pm61$ HV<sub>0.2/15</sub> for  $700^{\circ}$ C,  $850^{\circ}$ C, and 1000°C temperatures. The deviation in the CPTi-B<sub>4</sub>C-BN composition ranged from an asprocessed condition of  $527\pm51 \text{HV}_{0.2/15}$  to  $517\pm50 \text{HV}_{0.2/15}$ ,  $704\pm77 \text{HV}_{0.2/15}$  and  $647\pm76 \text{HV}_{0.2/15}$ for 700°C, 850°C, and 1000°C temperatures. Oxidized microstructures are shown in Figure 9. At 700°C, the oxidized B4C and BN reinforcement morphology resembles the as-processed state, namely, B4C with a slight reaction zone around the particles and TiB needles and TiC reinforcement forming perpendicular to the particles' surface. For the BN composition, the morphology resembles reacting BN particles with a network of TiN and TiB forming in the matrix, and a mixture of all reinforcing phases for the combined composition. At 850°C and 1000°C, however, the increase in the reaction zone length and reduction of B4C particle size is evident in the B4C reinforced composition (with white dotted lines indicating the increased thickness of the region). For the BN composition at 850°C, the amount of visible BN particles decreases, and at 1000°C there are no visible BN particles within the matrix, indicating that the reactions have continued during the high temperature testing.

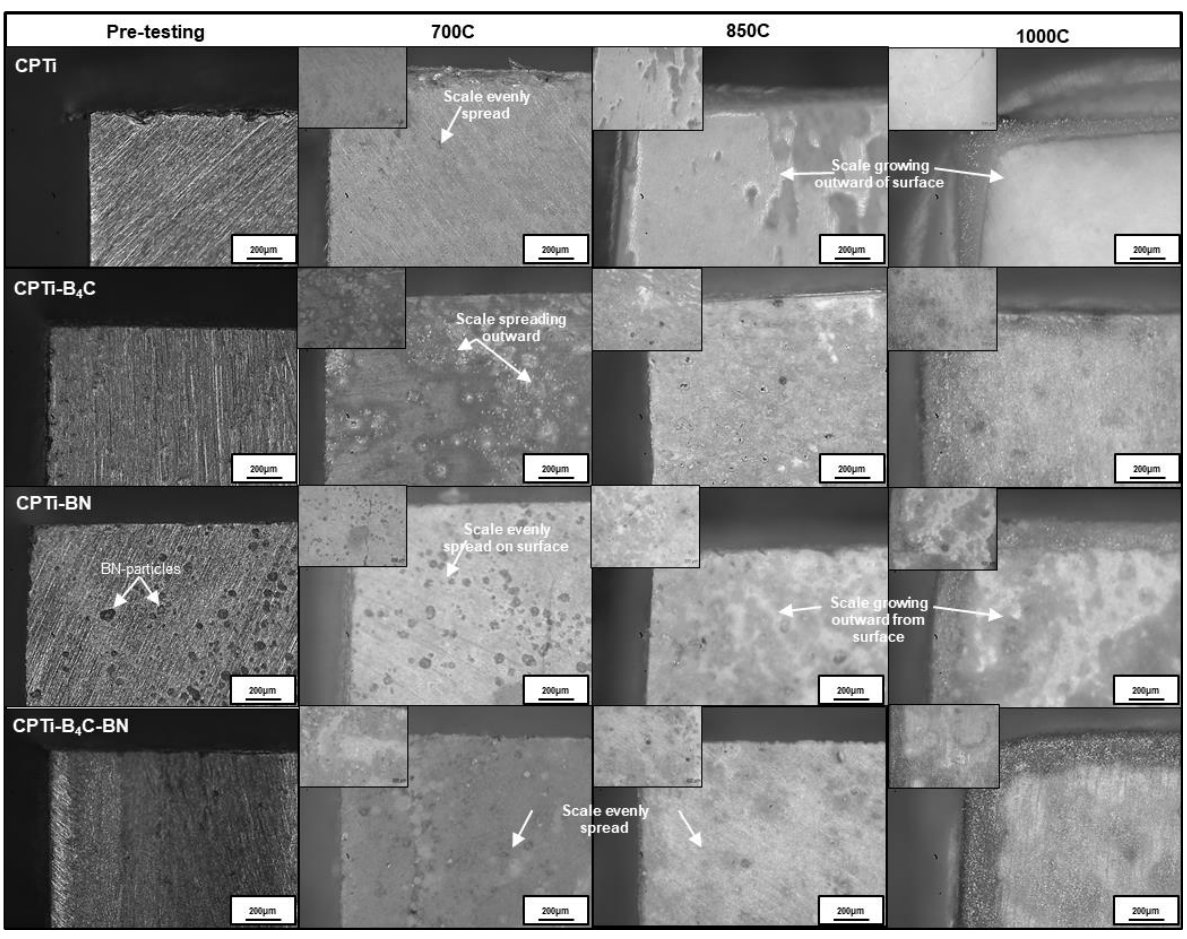


**Figure 6:** Surface morphological-evolution for 25-hour isothermally-oxidized samples at temperatures of 700°C, 850°C, and 1000°C (all tested for 25 hrs.), with the key scale characteristics outlined.

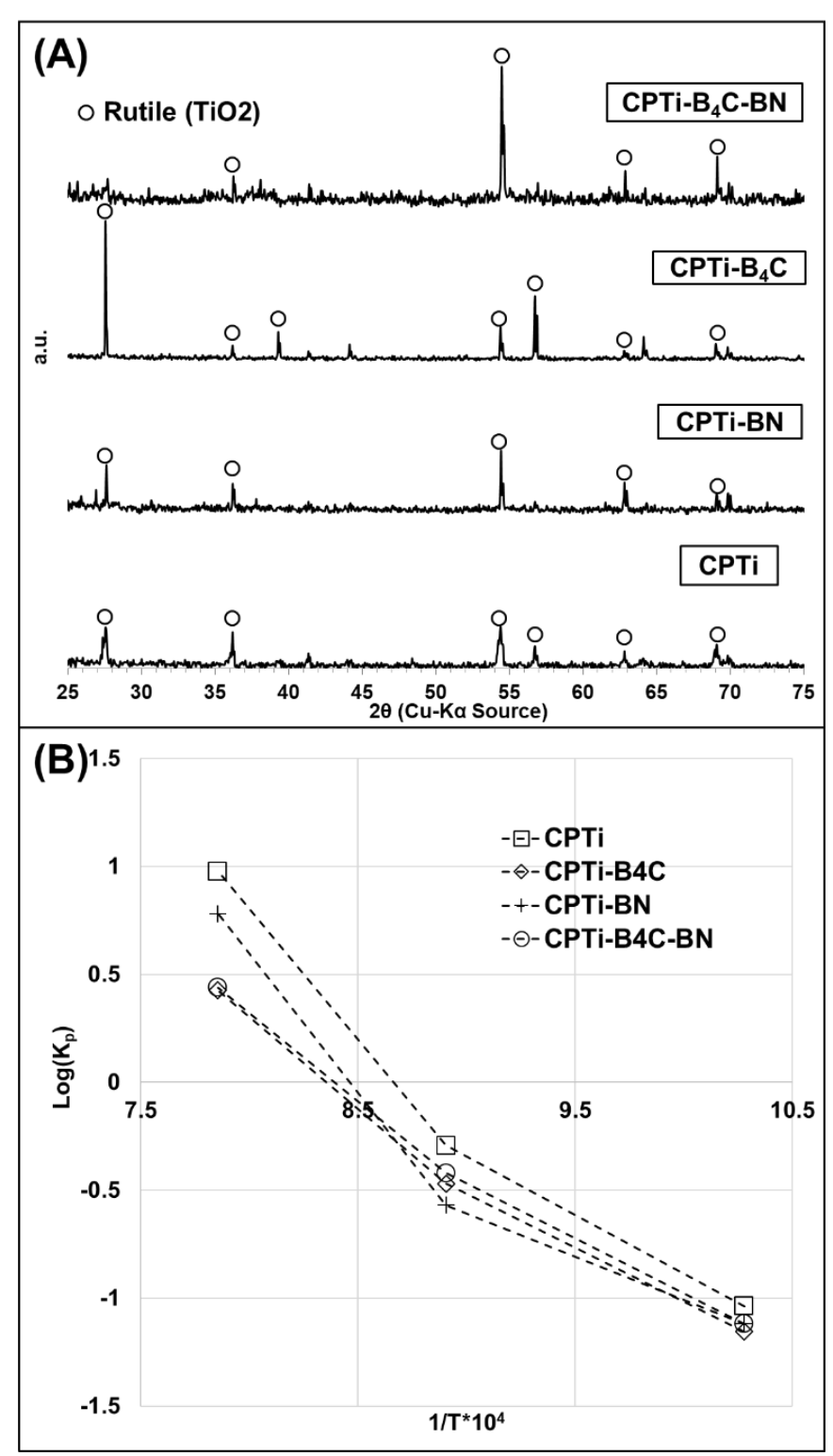


**Figure 7:** Oxide scale evolution analysis of each composite **(A)** XRD analysis of oxidized surface **(B)** Arrhenius plot using experimentally-determined Kp values.

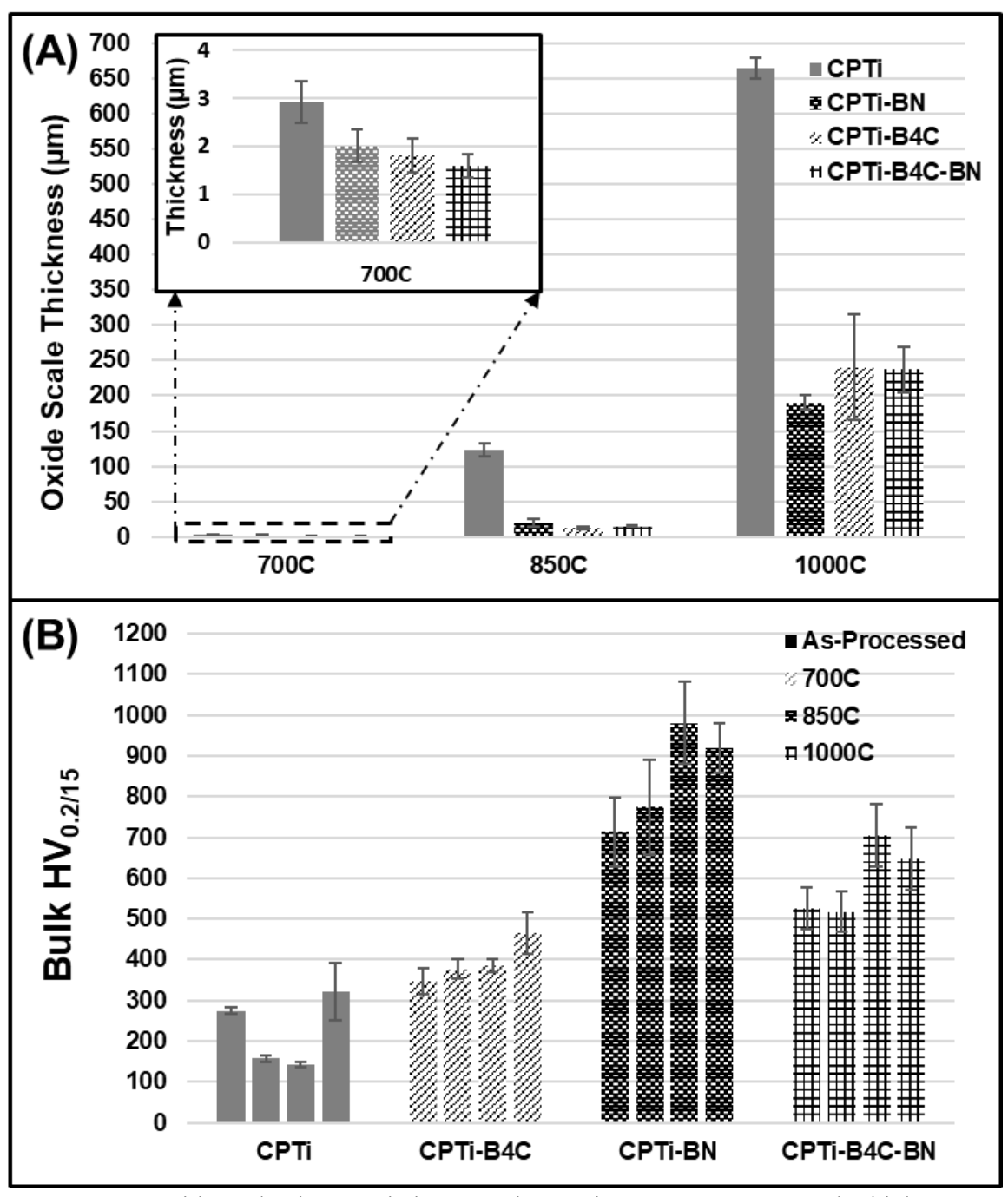


**Figure 8:** Oxide scale characteristics at each tested-temperature.(**A**) Scale thickness measurements (**B**) Bulk sample hardness (1.5mm from surface) comparison from as-processed to oxidized at different temperatures.

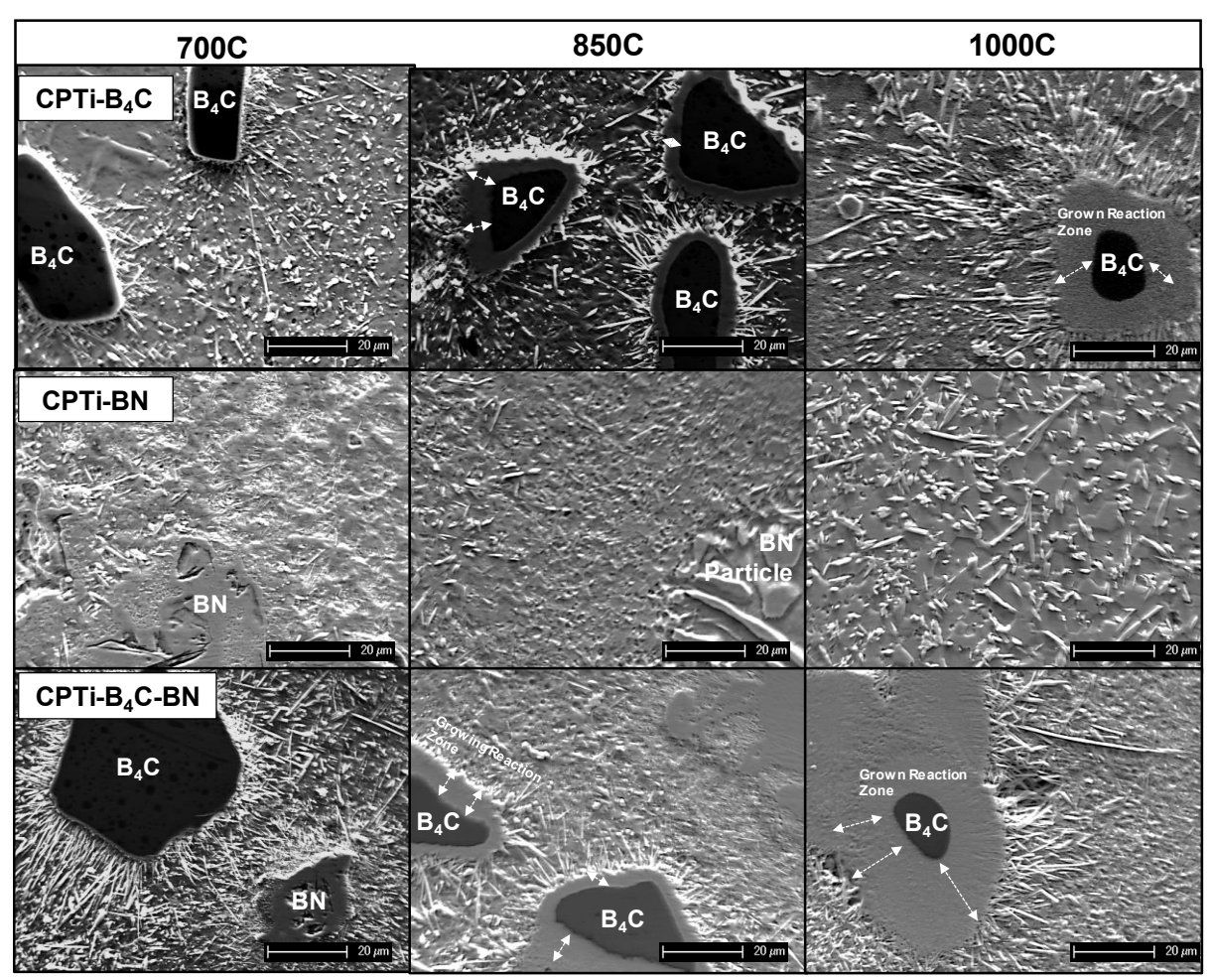


**Figure 9:** High magnification microstructures of oxidized reinforced-structures showing the phase evolution and continuation of *in situ* phase formation at different temperatures.

3.4 Thermomechanical and reciprocating-wear testing: Compression testing and thermal diffusivity analysis of the composites is shown in **Figs. 10 & 11**. For the CPTi composition, a compressive yield strength of 490±9MPa was achieved, with a modulus of 115±17GPa. B<sub>4</sub>C incorporation increased the strength by 43% to 700±20MPa, with only a 35% increase in

modulus (155±11GPa). Samples mainly failed through cracking in the reinforcement particles, with cracks being arrested by the titanium matrix for an overall ductile failure mode. BN incorporation, however, increased the modulus by as much as 56% to 179±11GPa with only a 24% increase in strength (609±7MPa). Failure for this composition mainly stemmed from cracks near small-scales pores in the BN particles and propagation through the matrix, initiating brittle failure (Fig. 11). The CPTi-B<sub>4</sub>C-BN composition demonstrated the highest strength (758±14MPa), a 55% increase in comparison to CPTi, with only a 33% increase in modulus (152±8GPa). As indicated from the damage cross sections, this composite failed through cracking in the reinforcement phase, with crack arrest by the CPTi matrix. No large-scale crack propagation was observed, leading to an overall ductile failure mode. From Fig. 10C, the thermal diffusivity of the CPTi matrix did not

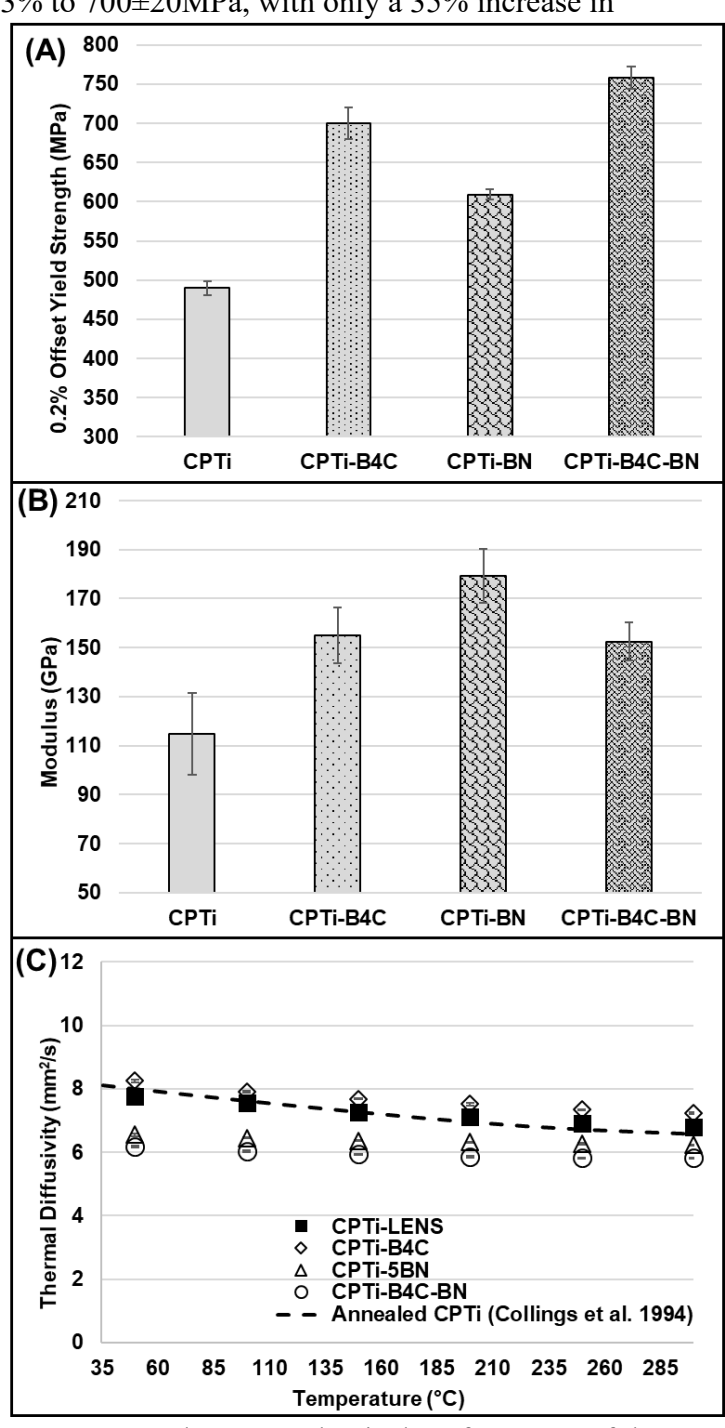


**Figure 10:** Thermomechanical performance of the composites. **(A)** Compression strength **(B)** Compressive modulus **(C)** Thermal diffusivity.

significantly differ compared to literature values, indicating that highly refined grain structure did not alter the thermal transport capability. Ceramic reinforcement had limited effect on

adjusting the thermal transport, with only 5-15% difference across 50°C-300°C, indicating that the titanium matrix material is the main thermal conductor. However, the B4C composition was much closer to the theoretical titanium values owing to its particle reinforcing nature. In the case of the BN-containing compositions, the reinforcement is both particle and in situ phase meaning that there is a

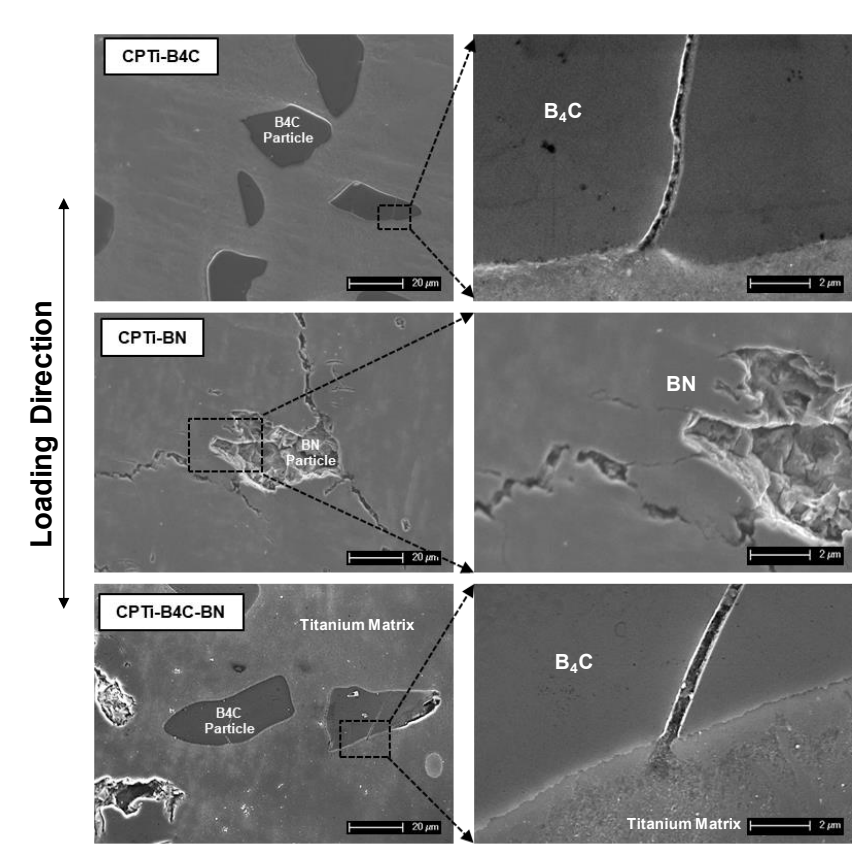


**Figure 11:** Damage analysis of ceramic-reinforced compression samples in low magnification (left column) and high magnification (right column).

higher degree of thermal resistance within the matrix for the conduction to take place, indicative of a lower thermal diffusivity as shown. Ceramic reinforcement significantly influenced the reciprocating-wear behavior of the composites (see **Fig. 12**). Both CPTi and CPTi-B<sub>4</sub>C compositions exhibited increasing coefficients of friction (COF) over reciprocating distance (beginning in the 0.4-0.5 range and increasing steadily past 1.2 at 1000m). The compound wear rates were  $0.59\pm0.04~(10^{-4}~\text{mm}3*\text{N}^{-1}*\text{m}^{-1})$  and  $0.38\pm0.0.01~(10^{-4}~\text{mm}3*\text{N}^{-1}*\text{m}^{-1})$ , respectively, indicating that the material removal was not significantly influenced by the incorporation of B<sub>4</sub>C. As shown in the tested surface micrographs (**Fig. 12B**), horizontal lines in the direction of testing as well as regions of gashing indicate the plastic deformation and "ploughing" material removal mechanism. The BN-containing compositions, however, maintained stable COF within the first 35-50m of testing (from 0.8-0.9 to 0.75-0.85 at 1000m). The significantly smaller wear track

diameters and limited evidence of gashing indicate its higher resistance to wear degradation. The compound wear rates for the CPTi-BN and CPTi-B<sub>4</sub>C-BN compositions were 0.17±0.003 (10<sup>-4</sup> mm3\*N<sup>-1</sup>\*m<sup>-1</sup>) and 0.12±0.0.010 (10<sup>-4</sup> mm3\*N<sup>-1</sup>\*m<sup>-1</sup>), respectively. Compared to titanium, these composites exhibited a 3.5X and 5X decrease in overall wear rate over the course of the 1000m test.

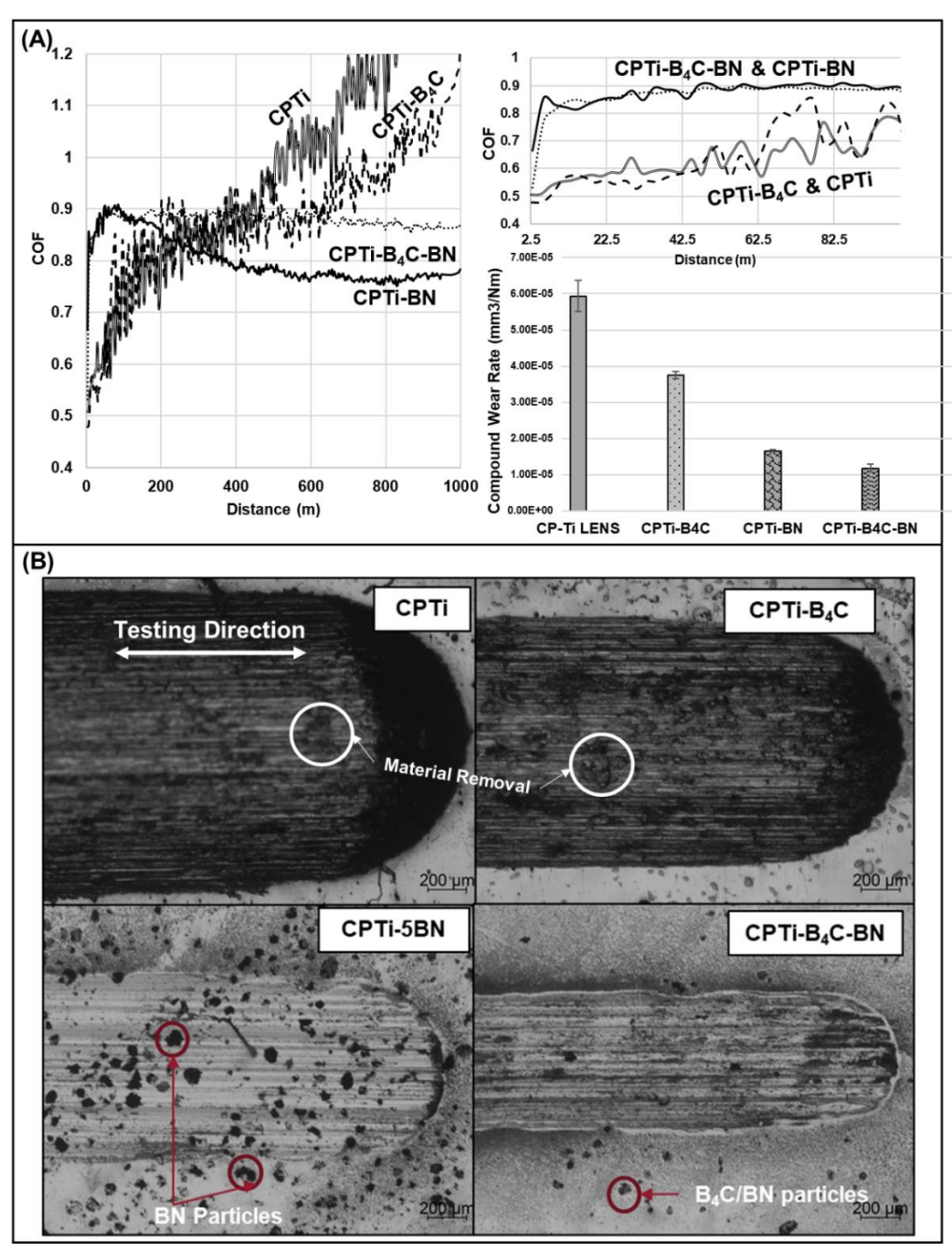


**Figure 12:** Wear performance of each composite. **(A)** COF and compound wear rates after 1000m **(B)** Micrographs of tested wear surfaces.

3.5 Manufacturing demonstration—tubular transition structures: Two strategies were utilized to join regions reinforced with strictly singular-ceramic reinforcement: direct joining and transitional joining using two layers of the CPTi-B<sub>4</sub>C-BN composition. For each printed composition, the optimized parameters from **Table 1** were utilized. From **Fig. 1**, it is shown that similar outer morphologies are achieved with both techniques in comparison to processing of the strictly-titanium tube, however, the hardness profiles across each structure show difference in the transition region (**Fig. 14A**). The final hardness values (900-1000HV for CPTi-BN and 200-300HV for the CPTi-B<sub>4</sub>C remain the same for both tubes, but the CPTi-B<sub>4</sub>C-BN intermediate-region tube maintains a plateau region as well as a diffuse interface region owing to the mixed composition deposition. In addition, the directly joined composition shows a steady increase in hardness along the height of the tube, without a plateau-region.

#### 4. Discussion

Reactive-deposition was previously investigated [11,12,29], however, the processing strategies and resulting mechanical properties of these materials are still not well understood. Because of this, the objective of this work was to understand the effects of individual and combinatorial reinforcement on the processing and properties of titanium-based metal matrix composites, with specific interest to the oxidation characteristics for high temperature applications.

4.1 Effect of ceramic on processing characteristics: Many factors contribute to a single material's processability using laser-based AM, which becomes more complex upon the introduction of multiple reinforcing phases into the powder mixture. Ideally, the laser-head standoff will remain at the same distance to the built sample on each layer (to maintain the laser focus spot), and processing parameters need to be optimized to achieve consistent melt characteristics and layer buildup for building an overall structure. As is the case here, the parameters that were used for CPTi were slightly different from the ceramic-reinforced compositions (350W vs. 410-450W), owing to the change in solidification characteristics (see Table 1). The increase in power was required to maintain the ~400μm layer thickness which was in the same range of 375-415μm among each composition. In our previous work [16], laser powers of 450W were used to maintain similar layer overall layer thicknesses, albeit for higher (10wt%) reinforcement of BN ceramic. In other works, similar laser power and processing

parameters were used for BN and/or B<sub>4</sub>C reinforced titanium [12,29]. In terms of dimensional expansion measurements relative to the CAD model, the averages ranged from 15.3%-18.9%, indicating that the achievable dimensional tolerancing is consistent across each composition, despite the addition of ceramic phase which complicates the melt pool characteristics. Other work has shown anywhere from 6-19% difference when incorporating ceramic phase into the titanium matrix, which is inadequate to be used for producing larger-scale components that require finer tolerances [16].

4.2 *In situ* reactivity, microstructure, and phase formations: The elevated temperatures experienced during DED-based processing can lead to reactions and significant phase evolution between feedstock materials [11,16]. The Gibbs free energy change for reactions between the metal (Ti) and the ceramic reinforcement (B<sub>4</sub>C/BN) can identify which phases are more likely to form during high-temperature processing. This analysis is carried out by evaluating the relative spontaneity of known reactions across a specified temperature range [38], and identifying which are more likely to occur. While this analysis does not consider time for diffusion, i.e. based solely on thermodynamic equilibrium (which is not the case in or around the melt pool), it can still identify insights into the nature of the reactions in the larger as-built structure. The Gibbs Free Energy change is defined by the fundamental relation:

$$\Delta G = \Delta H - T \Delta S \quad (7)$$

Where  $\Delta G$  is the free energy change for the given reaction (given in kJmol<sup>-1</sup>),  $\Delta H \& \Delta S$  are the enthalpy and entropy changes associated with the reaction (given in kJmol<sup>-1</sup> & kJmol<sup>-1</sup>K<sup>-1</sup>) and these are evaluated over a temperature range T. Previous investigations [29,38–42] have shown a multitude of relationships between titanium-boron nitride and titanium-boron carbide material systems using hot-pressing techniques, and the ones with the largest change in free energy are shown in **Table 4**.

**Table 4:** Gibbs Free Energy change analysis of reactants during reactive-deposition based processing

Reactants	Equation	$\Delta H \frac{kJ}{mol}$	$\Delta G \frac{kJ}{mol}$	Ref
Ti-BN	$3\text{Ti} + 2\text{BN} \rightarrow \text{TiB}_2 + 2\text{TiN} (4.1)$	-504	-446	[38,3 9]

	$2\text{Ti} + \text{BN} \rightarrow \text{TiB} + \text{TiN} (4.2)$	-256	-227	[24]
Ti-B <sub>4</sub> C 3'	$2\text{Ti} + \text{B}_4\text{C} \rightarrow 2\text{TiB}_2 + \text{C} (4.3)$	-594	-507	[43]
	$3\text{Ti} + \text{B}_4\text{C} \rightarrow 2\text{TiB}_2 + \text{TiC} (4.4)$	-780	-664	[24,3 8,43]
	$5\text{Ti} + \text{B}_4\text{C} \rightarrow 4\text{TiB} + \text{TiC} (4.5)$	-798	-710	[24,4 3,44]
Secondary	$Ti + TiB_2 \rightarrow 2TiB (4.6)$	-7	-6	[24,4 5,46]
Reactions		-1250	[38]	

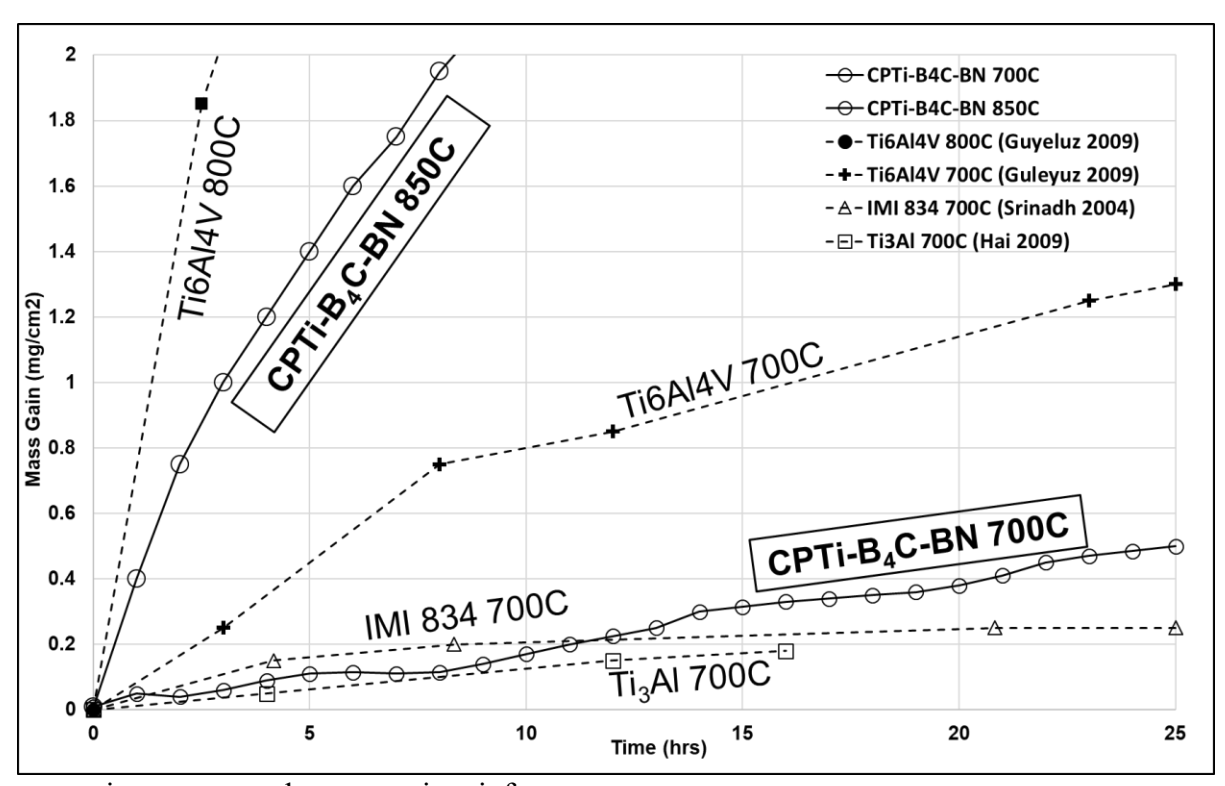
It should be noted that for the reported equations, the free energy change did not vary much throughout this temperature range, therefore the reported calculated values are averages. For the CPTi-BN system, Eqs. 4.1-4.2 indicate a free energy change from -227 kJmol<sup>-1</sup> to -446 kJmol<sup>-1</sup>, resulting in spontaneous formation of TiN and TiB/TiB<sub>2</sub> across the temperature range of 300-2300K. This agrees with the present findings from SEM imaging (dendritic TiN microstructures with TiB/TiB<sub>2</sub> networks interspersed throughout), as well as the phase analysis which identified both TiN and TiB phases present in the microstructure (Fig. 3). For the Ti-B<sub>4</sub>C system, Eqs. 4.3-4.5 indicate that the spontaneous reaction products across 300-2300K are TiB, TiC, and TiB<sub>2</sub>, with free energy change ranging from -507 kJmol<sup>-1</sup> to -710 kJmol<sup>-1</sup>. This is also in line with the TiC/TiB microstructures exhibited near the interface of Ti-B<sub>4</sub>C particles (Fig. 3). Eqs. 4.6 and 4.7 involve potential secondary reactions that can occur between feedstock materials. As has been previously reported [47], in situ TiB formation quickly follows the formation of TiB<sub>2</sub> when presented in an environment of abundant titanium, indicating that Eq. **4.6** is also involved with the formation of TiB in all three ceramic-containing compositions. Additionally, Eq. 4.7 indicates that during the phase evolution of the CPTi-B<sub>4</sub>C reaction zone, free carbon can help to drive the formation of TiB and TiC. When considering the combination composition (CPTi-B<sub>4</sub>C-BN), which exhibited microstructural characteristics of both the CPTi -BN and CPTi-B<sub>4</sub>C compositions, the lowest free energy change among all relationships are for Eqs. 4.7, 4.3, and 4.5, indicating that the theoretical formation of TiB<sub>2</sub>, TiC, and TiB are the most spontaneous. While these phases are present in the microstructure, it is clear that TiN is also a predominant phase in the microstructure, indicating that for this specific composition the analysis does not agree completely with our experiment. This is likely due to the fact that in the

melt pool (as well as very near to the melt pool) there are steep thermal gradients which significantly affect the reaction characteristics. Because BN particles have some internal porosity (**Fig. 3**) in comparison to the B<sub>4</sub>C particles, it is likely that the temperature and localized heating in those areas are higher than near the B<sub>4</sub>C particles. This would result in lower amounts of conductive pathways for heat transfer near the BN particles and cause more reaction to occur near to these particles, in comparison to the B<sub>4</sub>C particles.

4.3 Effect of ceramic reinforcement on thermal oxidation behavior: For each composition, thermal oxidation is a multi-factor phenomena governed by temperature, hold time, and environmental conditions. For titanium on its own, a material known for its affinity for oxygen which limits its temperature capability to 500-600°C in some cases, the issue is not only the surface scale growth than can cause cracking, but also the ingress of oxygen into the titanium lattice structure which can cause embrittlement and degradation of mechanical properties [48]. From the mass change curves (Fig. 5), it is clearly seen that the presence of ceramic reinforcement significantly influences the oxidation behavior at 850°C and 1000°C by decreasing the mass gain as well as the K<sub>p</sub> values by 45% to as high as 2.5X (250%), respectively. At 700°C all compositions exhibited a parabolic-breakaway regime indicative of a slow-growing uniform scale, where the oxide scale is beginning to form at points along the surface, but has yet to fully combine in different regions. This results in multiple regions where new growth takes place, and the resulting weight change is recorded. This changes as the ceramic reinforcement transitions this growth behavior from linear to parabolic at 850° and 1000°C, indicative of a slow-growing protective coating without spallation or cracking at high temperature. This is attributed mainly to the formation of dominant reinforcing phases such as TiN, TiB and TiB2, which have previously been shown to have a favorable effect on the oxidation behavior of titanium [49]. Not only do these phases prevent the formation of a scale on the surface, but also decrease the mobility of oxygen ingress and formation of "alpha-case" which is detrimental to the titanium lattice structure. This is especially the case at 1000°C, a temperature well above the β-transus where the BCC phase can provide higher mobility to the oxygen through the scale as well as into the bulk structure [49]. Despite the decrease in mass gain when exposed to high temperature, bulk hardness of the ceramic compositions is shown to increase overall when exposed to rising temperatures (Fig. 8B). This was mostly at temperatures

of 850°C and 1000°C, indicating that there is both phase evolution occurring during processing as well as during oxidation >850°C. This effect was most clear in the CPTi-BN composition which was shown to have a predominantly TiN and TiB microstructure, as well as high-reactivity during processing. It is clear that the reactions forming the *in situ* phases continued progressing when exposed to high temperature as was shown in [49], resulting in a more depleted titanium matrix and higher percentage of ceramic (and a correspondingly higher hardness). SEM micrographs in **Figure 9** indicate the continued reaction of both the BN and B4C reinforced compositions, whereby increased reaction zone thickness and the disappearance of the original BN particles is observed in the oxidized microstructures.

Understanding this phase evolution and effect on properties may be an important consideration for future work with the implications of component life when exposed to temperatures greater than 850°C. For the CPTi composition on its own, a decrease in hardness is shown at 700°C and 850°C likely due to annealing of the microstructure, but an increase at 1000°C likely due to the ingress of oxygen into the bulk structure and emphasizing the need for



protective agents such as ceramic reinforcement.

**Figure 13:** Mass gain of CPTi-B4C-BN composition in comparison to commercial alloys in the literature.

In comparison to literature of other commercial titanium alloys developed for high-temperature applications (**Fig. 13**), the CPTi-B<sub>4</sub>C-BN composition at 850°C outperformed Ti6Al4V tested at 800°C [50], and performed comparably in terms of mass gain to IMI-834 & Ti<sub>3</sub>Al at 700°C [51,52]. Although reporting lower Kp values, Hai et al. (2009) also reported oxide scales in the 3-5μm range for 800°C oxidized at 17hrs, indicating that the CPTi-B<sub>4</sub>C-BN composition (scale of 15.0±1.4μm at 850°C) maintained a similar overall scale thickness to the high-performance material developed with multiple alloying elements. In addition, both Hai et. al (2009) and Cvijovic-Alagic (2019) showed the formation of cracks in the combined Al<sub>2</sub>O<sub>3</sub>-TiO<sub>2</sub> scales owing to differences in the thermal expansion characteristics [53], indicating that the singular scale phase contributes to better adhesion to the base material.

4.4 Effect of ceramic reinforcement on thermomechanical and wear behavior: The properties of metal-ceramic composites are heavily influenced by their distribution of reinforcement phases, composition, and the processing methodology utilized [54,55]. While most composites can be analyzed from a rule-of-mixtures perspective, the in situ reactivity exhibited in the present work does not fully describe the properties of these composites. From a mechanical perspective, properties such as compressive modulus and strength are significantly affected by the nature of the reinforcing phases. For the CPTi-BN composition, the CPTi modulus was increased as high as 56% to 179±11GPa with only a 24% increase in strength owing to the formation of TiN (E~420GPa) and TiB (E~425-480GPa), which act in conjunction to increase the strength and modulus of the composite. However, large-scale cracks in the microstructure after compression failure indicate that this composition exhibits brittle characteristics. These were alleviated with the reduced amount of BN and introduction of B4C particles in the CPTi-B4C-BN composition, where failure mainly initiated through cracking in the reinforcement B4C phase as has been shown similar in [56], with crack arrest by the CPTi matrix and no crack propagation through the microstructure. This composition demonstrated the highest strength (758±14MPa), a 55% increase in comparison to CPTi, with only a 33% increase in modulus (152±8GPa) indicating that the combination of B4C and BN phases results in the greatest increases in strength at limited cost to ductility, while still maintaining the TiN and TiB phases that aid in wear-resistance. These values are comparable to other works involving TiB

reinforcement into titanium using powder metallurgical and/or self-propagating synthesis which result in strengths and moduli ranging from ~485-1100MPa depending on the amount of reinforcement and titanium alloy used as the matrix [54,57–59]. Namini et al. (2017) demonstrated a tensile strength as high as 485MPa with a 2.4wt% incorporation of TiB<sub>2</sub> into the titanium matrix using spark plasma sintering processing. Similar to the present work, grain refinement and reinforcement were shown to be the dominant reinforcing mechanisms [60]. From Fig. 10C, the thermal diffusivity of the CPTi matrix did not significantly differ compared to literature values, indicating that highly refined grain structure did not alter the thermal transport capability. Ceramic reinforcement had limited effect on adjusting the thermal transport, with only 5-15% difference across 50°C-300°C, indicating that the titanium matrix material is the main thermal conductor, and the introduction of reinforcing phases in small amounts does not compromise the thermal transport through the bulk structure as is typically the case with advanced high-temperature coatings.

Ceramic reinforcement significantly influenced the reciprocating-wear behavior of the composites (see Fig. 12). BN incorporation (and subsequent TiN and TiB phase formation) proved to maintained stable COFs within the first 35-50m of testing (from 0.8-0.9 to 0.75-0.85 at 1000m), and was also exhibited within the CPTi-B<sub>4</sub>C-BN composition. The significantly smaller wear track diameters and limited evidence of gashing indicate its higher resistance to wear degradation in the presence of the reciprocating load and in comparison to the titanium matrix. The compound wear rates for the CPTi-BN and CPTi-B<sub>4</sub>C-BN compositions were 0.17±0.003 (10<sup>-4</sup> mm3\*N<sup>-1</sup>\*m<sup>-1</sup>) and 0.12±0.0.010 (10<sup>-4</sup> mm3\*N<sup>-1</sup>\*m<sup>-1</sup>), respectively. Compared to titanium, these composites exhibited a 3.5X and 5X decrease in overall wear rate over the course of the 1000m test. In comparison to other works, the COF ranges were comparable to Traxel et al. (2018) which involved Ti-10wt%BN and COF ranging from 0.8-0.9 and limited wear debris exhibited throughout testing and hardness in the 1000-1400HV, as well as Sahasrabudhe et al. (2016) which featured an *in situ* nitride titanium surface and COF in the range of 0.7-0.9 during reciprocating wear testing with hardness as high as 1200-1400HV [61].

4.5 Future Directions: The combination of TiN, TiB and B<sub>4</sub>C phases in the CPTi-B<sub>4</sub>C-BN composition demonstrated a combination effect on the properties which resulted in the most desirable compression and wear testing, with acceptable oxidation performance and maintaining

similar thermal diffusivity to the titanium matrix. In some applications, it may be more desirable to have the TiN/TiB phases vs. the B<sub>4</sub>C phase so components such as those shown in Fig. 14 can be envisioned. The ability to tailor the structure in a single processing step significantly lowers

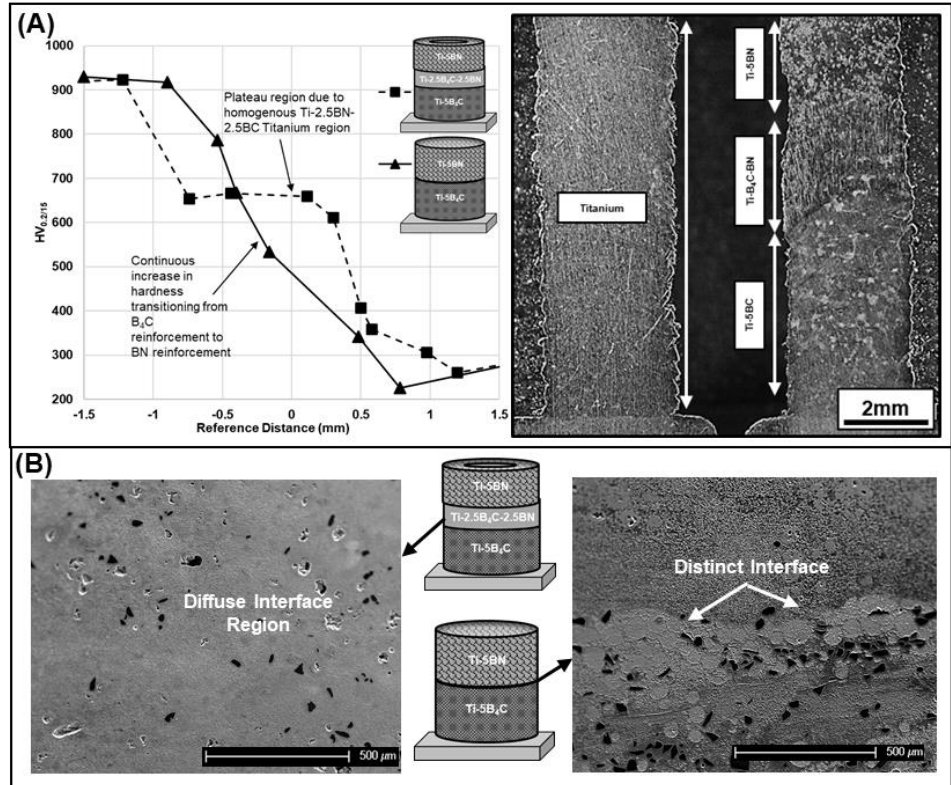


Figure 14: Functional reinforcement concept (A) Hardness profile and cross section micrograph (B) SEM interface characteristics.

costs for manufacturers of advanced components. Many different variant compositions can be envisioned, such as a higher loading of B<sub>4</sub>C that could further enhance the strength and oxidation resistance. Further, CPTi (unalloyed) material was used as the matrix in this study to understand the reactions of the feedstock powders with the base material, but it is envisioned that other additions of alloying elements could be used to further tailor the properties as has been shown in [12,16]. In addition, other reinforcing phases could be used to tailor the structural, biological, and/or thermal properties in different applications other than with the use of titanium.

# 5. Conclusions

Reactive-deposition based additive manufacturing was successfully employed to produce ceramic-reinforced titanium matrix composites with superior properties in comparison to the

base material, as well as site-specific reinforced structures. Multiphase microstructures comprised of titanium-based borides and nitrides were identified via SEM microstructural analysis and substantiated from XRD and Gibbs free energy analysis. BN-reinforcement significantly influenced the oxidation behavior from 700 to 1000°C, reducing the weight gain and scale thickness. Combined reinforcement significantly enhanced the strength and wear resistance at low cost to increasing the overall stiffness and propensity for brittle failure mode under loading. Our results indicate that combined ceramic-reinforcement via directed energy deposition can be exploited to enhance the material properties of commonly used materials such as titanium, as well as the ability to use a commercially-available additive manufacturing system to functionally reinforce a structure to achieve site-specific functionality.

# 6. Acknowledgements

Authors would like to acknowledge financial support from the National Science Foundation under the grant numbers NSF-CMMI 1538851 (PI - Bandyopadhyay) and NSF-CMMI 1934230 (PI - Bandyopadhyay), and the National Institute of Arthritis and Musculoskeletal and Skin Diseases of the National Institutes of Health under Award Number R01 AR067306-01A1. The content is solely the responsibility of the authors and does not necessarily represent the official views of the National Institutes of Health. Authors would also like experimental help from Dr. Jose Marcial and Emily Marcial of the N.O.M.E materials lab at WSU, as well as Dr. Thomas Williams from the University of Idaho for XRD assistance. Lab assistance from Bryan Heer, Jose D. Avila, Darin Malihi, Kyler Starkey, and Jesus (Jessi) Valladares is also greatly acknowledged.

#### 7. Declaration of Interest

The authors declare no conflict of interest.

## 8. References

[1] J.H. Martin, B.D. Yahata, J.M. Hundley, J.A. Mayer, T.A. Schaedler, T.M. Pollock, 3D printing of high-strength aluminium alloys, Nature. 549 (2017) 365–369. doi:10.1038/nature23894.

- [2] D. Bowden, Y. Krysiak, L. Palatinus, D. Tsivoulas, S. Plana-Ruiz, E. Sarakinou, U. Kolb, D. Stewart, M. Preuss, A high-strength silicide phase in a stainless steel alloy designed for wear-resistant applications, Nat. Commun. 9 (2018). doi:10.1038/s41467-018-03875-9.
- [3] T. DebRoy, H.L. Wei, J.S. Zuback, T. Mukherjee, J.W. Elmer, J.O. Milewski, A.M. Beese, A. Wilson-Heid, A. De, W. Zhang, Additive manufacturing of metallic components Process, structure and properties, Prog. Mater. Sci. 92 (2018) 112–224. doi:10.1016/j.pmatsci.2017.10.001.
- [4] A.M. Beese, Z. Wang, A.D. Stoica, D. Ma, Absence of dynamic strain aging in an additively manufactured nickel-base superalloy, Nat. Commun. 9 (2018). doi:10.1038/s41467-018-04473-5.
- [5] D.C. Hofmann, S. Roberts, R. Otis, J. Kolodziejska, R.P. Dillon, J.O. Suh, A.A. Shapiro, Z.K. Liu, J.P. Borgonia, Developing gradient metal alloys through radial deposition additive manufacturing, Sci. Rep. 4 (2014). doi:10.1038/srep05357.
- [6] A. Bandyopadhyay, K.D. Traxel, Invited review article: Metal-additive manufacturing—Modeling strategies for application-optimized designs, Addit. Manuf. 22 (2018) 758–774. doi:10.1016/j.addma.2018.06.024.
- [7] E. MacDonald, R. Wicker, Multiprocess 3D printing for increasing component functionality, Science (80-.). (2016). doi:10.1126/science.aaf2093.
- [8] X. Wang, S. Xu, S. Zhou, W. Xu, M. Leary, P. Choong, M. Qian, M. Brandt, Y.M. Xie, S.X. Xiaojian Wang Shiwei Zhou, Wei Xu, Martin Leary, Peter Choong, M. Qian, Milan Brandt, Yi Min Xie., X. Wang, S. Xu, S. Zhou, W. Xu, M. Leary, P. Choong, M. Qian, M. Brandt, Y.M. Xie, S.X. Xiaojian Wang Shiwei Zhou, Wei Xu, Martin Leary, Peter Choong, M. Qian, Milan Brandt, Yi Min Xie., X. Wang, S. Xu, S. Zhou, W. Xu, M. Leary, P. Choong, M. Qian, M. Brandt, Y.M. Xie, Topological design and additive manufacturing of porous metals for bone scaffolds and orthopaedic implants: A review, Biomaterials. 83 (2016) 127–141. doi:10.1016/j.biomaterials.2016.01.012.
- [9] P. Zhang, J. Liu, A.C. To, Role of anisotropic properties on topology optimization of additive manufactured load bearing structures, Scr. Mater. 135 (2017) 148–152. doi:10.1016/j.scriptamat.2016.10.021.
- [10] A. Bandyopadhyay, H. Sahasrabudhe, S. Bose, Reactive deposition systems and associated methods, US20170247785A1, 2014.
- [11] H. Sahasrabudhe, A. Bandyopadhyay, Additive Manufacturing of Reactive In Situ Zr Based Ultra-High Temperature Ceramic Composites, Jom. 68 (2016) 822–830. doi:10.1007/s11837-015-1777-x.
- [12] M. Das, V.K. Balla, D. Basu, I. Manna, T.S. Sampath Kumar, A. Bandyopadhyay, Laser processing of in situ synthesized TiB-TiN-reinforced Ti6Al4V alloy coatings, Scr. Mater. 66 (2012) 578–581. doi:10.1016/j.scriptamat.2012.01.010.
- [13] T. Kühnle, K. Partes, In-Situ Formation of Titanium Boride and Titanium Carbide by Selective Laser Melting, in: Phys. Procedia, 2012: pp. 432–438. doi:10.1016/j.phpro.2012.10.058.

- [14] H. Attar, M. Bönisch, M. Calin, L.C. Zhang, S. Scudino, J. Eckert, Selective laser melting of in situ titanium-titanium boride composites: Processing, microstructure and mechanical properties, Acta Mater. 76 (2014) 13–22. doi:10.1016/j.actamat.2014.05.022.
- [15] F.A.P. Fernandes, J. Gallego, C.A. Picon, G. Tremiliosi Filho, L.C. Casteletti, Wear and corrosion of niobium carbide coated AISI 52100 bearing steel, Surf. Coatings Technol. 279 (2015) 112–117. doi:10.1016/j.surfcoat.2015.08.036.
- [16] K.D. Traxel, A. Bandyopadhyay, Reactive-deposition-based additive manufacturing of Ti-Zr-BN composites, Addit. Manuf. 24 (2018). doi:10.1016/j.addma.2018.10.005.
- [17] W. Pompe, H. Worch, M. Epple, W. Friess, M. Gelinsky, P. Greil, U. Hempel, D. Scharnweber, K. Schulte, Functionally graded materials for biomedical applications, Mater. Sci. Eng. A. 362 (2003) 40–60. doi:10.1016/S0921-5093(03)00580-X.
- [18] A. Sola, D. Bellucci, V. Cannillo, Functionally graded materials for orthopedic applications an update on design and manufacturing, Biotechnol. Adv. 34 (2016) 504–531. doi:10.1016/j.biotechadv.2015.12.013.
- [19] B. Vamsi Krishna, W. Xue, S. Bose, A. Bandyopadhyay, Functionally graded Co-Cr-Mo coating on Ti-6Al-4V alloy structures, Acta Biomater. 4 (2008) 697–706. doi:10.1016/j.actbio.2007.10.005.
- [20] E.W. Collings, The Physical Metallurgy of Titanium Alloys, ASM Series in Metal Processing, 1986.
- [21] M.N. Mungole, N. Singh, G.N. Mathur, Oxidation behaviour of Ti6Al4V titanium alloy in oxygen, Mater. Sci. Technol. 18 (2002) 111–114. doi:10.1179/026708301125000302.
- [22] H. Attar, S. Ehtemam-Haghighi, D. Kent, M.S. Dargusch, Recent developments and opportunities in additive manufacturing of titanium-based matrix composites: A review, Int. J. Mach. Tools Manuf. 133 (2018) 85–102. doi:10.1016/j.ijmachtools.2018.06.003.
- [23] Q. An, L.J. Huang, Y. Bao, R. Zhang, S. Jiang, L. Geng, M. Xiao, Dry sliding wear characteristics of in-situ TiBw/Ti6Al4V composites with different network parameters, Tribol. Int. 121 (2018) 252–259. doi:10.1016/j.triboint.2018.01.053.
- [24] M. Yi, X. Zhang, G. Liu, B. Wang, H. Shao, G. Qiao, Comparative investigation on microstructures and mechanical properties of (TiB + TiC)/Ti-6Al-4V composites from Ti-B4C-C and Ti-TiB2-TiC systems, Mater. Charact. (2018). doi:10.1016/j.matchar.2018.04.010.
- [25] S. Ghesmati Tabrizi, S.A. Sajjadi, A. Babakhani, W. Lu, Influence of spark plasma sintering and subsequent hot rolling on microstructure and flexural behavior of in-situ TiB and TiC reinforced Ti6Al4V composite, Mater. Sci. Eng. A. 624 (2015) 271–278. doi:10.1016/j.msea.2014.11.036.
- [26] B. Haldar, S. Karmakar, P. Saha, A.B. Chattopadhyay, In situ multicomponent MMC coating developed on Ti–6Al–4V substrate, Surf. Eng. (2014). doi:10.1179/1743294414y.0000000252.
- [27] C. Lin, Y. Han, C. Guo, Y. Chang, X. Han, L. Lan, F. Jiang, Synthesis and mechanical

- properties of novel Ti-(SiCf/Al3Ti) ceramic-fiber-reinforced metal-intermetallic-laminated (CFR-MIL) composites, J. Alloys Compd. 722 (2017) 427–437. doi:10.1016/j.jallcom.2017.06.057.
- [28] C.J. Zhang, F.T. Kong, S.L. Xiao, E.T. Zhao, L.J. Xu, Y.Y. Chen, Evolution of microstructure and tensile properties of in situ titanium matrix composites with volume fraction of (TiB+TiC) reinforcements, Mater. Sci. Eng. A. 548 (2012) 152–160. doi:10.1016/j.msea.2012.04.004.
- [29] M. Das, K. Bhattacharya, S.A. Dittrick, C. Mandal, V.K. Balla, T.S. Sampath Kumar, A. Bandyopadhyay, I. Manna, In situ synthesized TiB-TiN reinforced Ti6Al4V alloy composite coatings: Microstructure, tribological and in-vitro biocompatibility, J. Mech. Behav. Biomed. Mater. 29 (2014) 259–271. doi:10.1016/j.jmbbm.2013.09.006.
- [30] A. Uriondo, M. Esperon-Miguez, S. Perinpanayagam, The present and future of additive manufacturing in the aerospace sector: A review of important aspects, Proc. Inst. Mech. Eng. Part G J. Aerosp. Eng. 229 (2015) 2132–2147. doi:10.1177/0954410014568797.
- [31] ASTM Standard E384-16, Test Method for Microindentation Hardness of Materials, ASTM International, West Conshohocken, PA, PA, 2016. doi:10.1520/E0384-16.
- [32] ASTM Standard C1327, W. Conshohocken, ASTM Standard C1327, Test Method for Vickers Indentation Hardness of Advanced Ceramics, ASTM International, West Conshohocken, PA, PA, 2015. doi:10.1520/C1327-08.2.
- [33] ASTM Standard E9-09, Standard Test Methods of Compression Testing of Metallic Materials at Room Temperature, Annu. B. ASTM Stand. 3.01 (2012) 92–100. doi:10.1520/E0009-09.2.
- [34] ASTM Standard G-133-05, Test Method for Linearly Reciprocating Ball-on-Flat Sliding Wear, ASTM International, West Conshohocken, PA, PA, 2016. doi:10.1520/G0133-05R10.2.
- [35] S. Li, K. Kondoh, H. Imai, B. Chen, L. Jia, J. Umeda, Y. Fu, Strengthening behavior of in situ-synthesized (TiC TiB)/Ti composites by powder metallurgy and hot extrusion, Jmade. 95 (2016) 127–132. doi:10.1016/j.matdes.2016.01.092.
- [36] H. Guleryuz, H. Cimenoglu, Oxidation of Ti–6Al–4V alloy, J. Alloys Compd. 472 (2009) 241–246. doi:10.1016/j.jallcom.2008.04.024.
- [37] S. Frangini, A. Mignone, F. de Riccardis, Various aspects of the air oxidation behaviour of a Ti6Al4V alloy at temperatures in the range 600-700 °C, J. Mater. Sci. (1994). doi:10.1007/BF00445984.
- [38] G.J. Zhang, M. Ando, J.F. Yang, T. Ohji, S. Kanzaki, Boron carbide and nitride as reactants for in situ synthesis of boride-containing ceramic composites, J. Eur. Ceram. Soc. 24 (2004) 171–178. doi:10.1016/S0955-2219(03)00607-1.
- [39] G. V. Samsonov, A.L. Burykina, O.A. Medvedeva, V.P. Kosteruk, Reactions of boron nitride with transition metals and their borides and nitrides, Sov. Powder Metall. Met. Ceram. 12 (1973) 903–908. doi:10.1007/BF00794628.

- [40] H. Zhao, J. Wang, Z. Zhu, J. Wang, W. Pan, Mechanical properties and microstructure of in situ synthesized ZrB2-ZrN1-x composites, J. Mater. Sci. 41 (2006) 1769–1773. doi:10.1007/s10853-006-2870-x.
- [41] B. Sarma, N.M. Tikekar, K.S. Ravi Chandran, Kinetics of growth of superhard boride layers during solid state diffusion of boron into titanium, Ceram. Int. 38 (2012) 6795–6805. doi:10.1016/j.ceramint.2012.05.077.
- [42] J. Morgiel, E. Benko, Microstructure of boron nitride sintered with titanium, Mater. Lett. 25 (1995) 49–52. doi:10.1016/0167-577X(95)00138-7.
- [43] M.O. Ogunlana, E.T. Akinlabi, M.F. Erinosho, Analysis of the influence of laser power on the microstructure and properties of a titanium alloy-reinforced boron carbide matrix composite (Ti6Al4V-B4C), Stroj. Vestnik/Journal Mech. Eng. (2017). doi:10.5545/sv-jme.2016.4159.
- [44] J. Zhang, W. Ke, W. Ji, Z. Fan, W. Wang, Z. Fu, Microstructure and properties of insitu titanium boride (TiB)/titanium (TI) composites, Mater. Sci. Eng. A. 648 (2015) 158–163. doi:10.1016/j.msea.2015.09.067.
- [45] K.B. Panda, K.S.R. Chandran, First principles determination of elastic constants and chemical bonding of titanium boride (TiB) on the basis of density functional theory, Acta Mater. 54 (2006) 1641–1657. doi:10.1016/j.actamat.2005.12.003.
- [46] S. Mischler, Triboelectrochemical techniques and interpretation methods in tribocorrosion: A comparative evaluation, Tribol. Int. 41 (2008) 573–583. doi:10.1016/j.triboint.2007.11.003.
- [47] A. Sabahi Namini, M. Azadbeh, Microstructural characterisation and mechanical properties of spark plasma-sintered TiB 2 -reinforced titanium matrix composite, Powder Metall. 60 (2017) 22–32. doi:10.1080/00325899.2016.1265805.
- [48] J. Dai, J. Zhu, C. Chen, F. Weng, High temperature oxidation behavior and research status of modifications on improving high temperature oxidation resistance of titanium alloys and titanium aluminides: A review, J. Alloys Compd. 685 (2016) 784–798. doi:10.1016/j.jallcom.2016.06.212.
- [49] J.D. Avila, A. Bandyopadhyay, Influence of boron nitride on reinforcement to improve high temperature oxidation resistance of titanium, J. Mater. Res. (2019) 1–11. doi:10.1557/jmr.2019.11.
- [50] H. Guleryuz, H. Cimenoglu, Oxidation of Ti–6Al–4V alloy, J. Alloys Compd. 472 (2009) 241–246. doi:10.1016/j.jallcom.2008.04.024.
- [51] K.V.S. Srinadh, V. Singh, Oxidation behaviour of the near α-titanium alloy IMI 834, Bull. Mater. Sci. (2004).
- [52] Y. hai QIAN, M. shuan LI, B. LU, Isothermal oxidation behavior of Ti3Al-based alloy at 700-1000 °C in air, Trans. Nonferrous Met. Soc. China (English Ed. (2009). doi:10.1016/S1003-6326(08)60306-4.
- [53] I. Cvijović-Alagić, Z. Cvijović, D. Zagorac, M.T. Jovanović, Cyclic oxidation of Ti3Al-

- based materials, Ceram. Int. 45 (2019) 9423–9438. doi:10.1016/j.ceramint.2018.08.287.
- [54] M.D. Hayat, H. Singh, Z. He, P. Cao, Titanium metal matrix composites: An overview, Compos. Part A Appl. Sci. Manuf. 121 (2019) 418–438. doi:10.1016/j.compositesa.2019.04.005.
- [55] H. Attar, S. Ehtemam-Haghighi, D. Kent, M.S. Dargusch, Recent developments and opportunities in additive manufacturing of titanium-based matrix composites: A review, Int. J. Mach. Tools Manuf. 133 (2018) 85–102. doi:10.1016/j.ijmachtools.2018.06.003.
- [56] J. Wang, L. Li, P. Lin, J. Wang, Effect of TiC particle size on the microstructure and tensile properties of TiCp/Ti6Al4V composites fabricated by laser melting deposition, Opt. Laser Technol. 105 (2018) 195–206. doi:10.1016/j.optlastec.2018.03.009.
- [57] H.T. Tsang, G.G. Chao, C.Y. Ma, Effects of volume fraction of reinforcement on tensile and creep properties of in-situ TiB/Ti MMC, Scr. Mater. (1997). doi:10.1016/S1359-6462(97)00251-0.
- [58] X. Zhang, Q. Xu, J. Han, V.L. Kvanin, Self-propagating high temperature combustion synthesis of TiB/Ti composites, Mater. Sci. Eng. A. (2003). doi:10.1016/S0921-5093(02)00635-4.
- [59] M. Ozerov, M. Klimova, A. Kolesnikov, N. Stepanov, S. Zherebtsov, Deformation behavior and microstructure evolution of a Ti/TiB metal-matrix composite during high-temperature compression tests, Mater. Des. 112 (2016) 17–26. doi:10.1016/j.matdes.2016.09.051.
- [60] A. Sabahi Namini, M. Azadbeh, Microstructural characterisation and mechanical properties of spark plasma-sintered TiB 2 -reinforced titanium matrix composite, Powder Metall. 60 (2017) 22–32. doi:10.1080/00325899.2016.1265805.
- [61] H. Sahasrabudhe, J. Soderlind, A. Bandyopadhyay, Laser processing of in situ TiN/Ti composite coating on titanium, J. Mech. Behav. Biomed. Mater. 53 (2016) 239–249. doi:10.1016/j.jmbbm.2015.08.013.